J. Fluid Mech. (2014), *vol.* 745, *pp.* 509–536.
doi:10.1017/jfm.2014.105

Multi-oscillations of a bubble in a compressible liquid near a rigid boundary

Qianxi Wang†

School of Mathematics, University of Birmingham, Birmingham B15 2TT, UK

(Received 24 May 2013; revised 13 January 2014; accepted 20 February 2014;
first published online 24 March 2014)

Bubble dynamics near a rigid boundary are associated with wide and important applications in cavitation erosion in many industrial systems and medical ultrasonics. This classical problem is revisited with the following two developments. Firstly, computational studies on the problem have commonly been based on an incompressible fluid model, but the compressible effects are essential in this phenomenon. Consequently, a bubble usually undergoes significantly damped oscillation in practice. In this paper this phenomenon will be modelled using weakly compressible theory and a modified boundary integral method for an axisymmetric configuration, which predicts the damped oscillation. Secondly, the computational studies so far have largely been concerned with the first cycle of oscillation. However, a bubble usually oscillates for a few cycles before it breaks into much smaller ones. Cavitation erosion may be associated with the recollapse phase when the bubble is initiated more than the maximum bubble radius away from the boundary. Both the first and second cycles of oscillation will be modelled. The toroidal bubble formed towards the end of the collapse phase is modelled using a vortex ring model. The repeated topological changes of the bubble are traced from a singly connected to a doubly connected form, and vice versa. This model considers the energy loss due to shock waves emitted at minimum bubble volumes during the beginning of the expansion phase and around the end of the collapse phase. It predicts damped oscillations, where both the maximum bubble radius and the oscillation period reduce significantly from the first to second cycles of oscillation. The damping of the bubble oscillation is alleviated by the existence of the rigid boundary and reduces with the standoff distance between them. Our computations correlate well with the experimental data (Philipp & Lauterborn, *J. Fluid Mech.*, vol. 361, 1998, pp. 75–116) for both the first and second cycles of oscillation. We have successively reproduced the bubble ring in direct contact with the rigid boundary at the end of the second collapse phase, a phenomenon that was suggested to be one of the major causes of cavitation erosion by experimental studies.

Key words: bubble dynamics, cavitation, drops and bubbles

1. Introduction

Bubble dynamics in the neighbourhood of a rigid boundary is a classical problem. Traditional research into this topic has generally been associated with the mechanism

† Email address for correspondence: Q.X.Wang@bham.ac.uk

of cavitation erosion in many industrial systems, such as ship propellers, turbines, pipelines and cryogenic pumps (Rayleigh 1917; Taylor 1942; Plesset & Prosperetti 1977; Blake & Gibson 1987; Young 1989; Leighton 1994; Brennen 1995). These continue to remain important application areas, and the challenge still stands, since cavitation erosion still presents a problem and its mechanism has not yet been fully elucidated (Lauterborn & Kurz 2010).

Recent research into the bubble–boundary interaction is associated with important medical applications, including extracorporeal shock wave lithotripsy (Klaseboer *et al.* 2007; Calvisi, Iloreta & Szeri 2008; Iloreta, Fung & Szeri 2008), tissue ablating (histotripsy) (Roberts *et al.* 2006; Coussios & Roy 2007), and oncology and cardiology (Leslie & Kennedy 2006). Erosion mechanisms of cavitation are widely utilized in ultrasound cavitation cleaning – one of the most effective cleaning processes for electrical and medical micro-devices (Song *et al.* 2004).

Extensive experiments have been conducted for bubble dynamics near a plane rigid boundary using focused laser light or electric sparks for generation of a bubble and high-speed photography for recording bubble evolution. A shock wave originates from a strong compression of the bubble content at the starting of a gas bubble (Tomita & Shima 1986; Philipp & Lauterborn 1998). This is followed by growth and collapse of the bubble. Near the end of the collapse phase, a high-speed liquid jet directed towards the rigid boundary forms. Bubble jetting was suggested intuitively by Kornfeld & Suvorov (1944), noticed experimentally by Naudé & Ellis (1961) and first simulated by Plesset & Chapman (1971).

The shock wave propagates in a much smaller time scale than the bubble oscillation, so the two phenomena are usually modelled separately. The shock wave is modelled using a compressible model, and the bubble dynamics is largely modelled using an incompressible model. The inviscid model based on the boundary integral method (BIM) is grid-free in the flow domain and has been widely used in bubble boundary interactions for axisymmetric cases (Lenoir 1979; Guerri, Lucca & Prosperetti 1981; Blake, Taib & Doherty 1986, 1987; Blake *et al.* 1997; Brujan *et al.* 2002; Szeri *et al.* 2003; Pearson, Blake & Otto 2004; Lind & Phillips 2012; Curtiss *et al.* 2013; Wang *et al.* 2013) and for three-dimensional configurations (Chahine & Bovis 1980; Chahine & Perdue 1988; Duncan, Milligan & Zhang 1996; Chahine & Harris 1998*a*,*b*; Wang 1998, 2004; Klaseboer *et al.* 2005; Jayaprakash, Chao-Tsung & Chahine 2010; Jayaprakash, Singh & Chahine 2011).

Bubble dynamics near a rigid boundary have also been simulated using domain approaches coupled with various interface-capturing schemes (Yu, Ceccio & Tryggvason 1995; Popinet & Zaleski 2002; Turangan *et al.* 2008; Minsier, De Wilde & Proost 2009) based on the Euler equation or Navier–Stokes equations for axisymmetric configuration. Other domain approaches to bubble dynamics include Wardlaw & Luton (2000), Wardlaw *et al.* (2003*a*,*b*), Bonometti & Magnaudet (2007), Hua & Lou (2007), Yue *et al.* (2007), Johnsen & Colonius (2008), Yang & Prosperetti (2008), Adoua, Legendre & Magnaudet (2009), Johnsen & Colonius (2009) and Bonhomme *et al.* (2012).

The above separated modelling of the shock wave and bubble dynamics works only before the end of the collapse phase, when shock waves are often generated again by strong compression of the bubble content and/or jet impact. A significant part of the energy of the bubble system will be lost due to the generation and propagation of shock waves. As a result, the maximum volume and oscillation period of the bubble reduce significantly from the first cycle of oscillation to the second cycle (Tomita & Shima 1986; Philipp & Lauterborn 1998). A compressible model has to be used to simulate both the shock wave and bubble dynamics at the end of collapse.

The radial dynamics of spherical bubbles in compressible fluids have been studied extensively for many decades (Herring 1941; Keller & Kolodner 1956). Prosperetti & Lezzi (1986) and Lezzi & Prosperetti (1987) modelled spherical bubble dynamics in a compressible liquid by using matched asymptotic expansions. They proved the well-known Herring equation. Geers & Zhang (1994), Geers & Hunter (2002) and Geers, Lagumbay & Vasilyev (2012) employed the doubly asymptotic approximations for spherical bubble dynamics for both the external liquid and the internal gas. They noticed that, while acoustic-wave effects in the external liquid are important, such effects in the internal gas are not.

Few computational studies consider the compressible effects in non-spherical bubble dynamics. Lee, Klaseboer & Khoo (2007) modified the BIM by empirically removing a part of the bubble potential energy at the end of the first cycle of oscillation, since there were no suitable methods for predicting the energy loss of a bubble system associated with non-spherical bubble collapse. Wang & Blake (2010, 2011) developed a weakly compressible bubble theory for non-spherical cavitation microbubbles when subjected to travelling and standing waves. Wang (2013) simulated underwater explosion bubble dynamics subject to buoyancy using a weakly compressible theory.

The first objective of this paper is to study bubble dynamics near a rigid boundary in a compressible liquid. We will model this phenomenon based on a weakly compressible theory, because the associated liquid flow is often associated with a low Mach number, including at the moment when the shock wave is generated. It has been confirmed from many experiments in the literature that the maximum velocity of a boundary-induced bubble jet is lower than 200 m s^{-1} at normal ambient pressure (Philipp & Lauterborn 1998). Note that a shock wave in bubble dynamics may or may not be associated with a supersonic flow, which is a different concept from a shock wave in aerodynamics; the latter is always associated with a supersonic flow. In addition, Geers *et al.* (2012) compared weakly compressible theory with the numerical solution for the Euler equation for spherical bubbles for large parameter ranges. They noticed that weakly compressible theory provides very accurate results.

Weakly compressible theory is invalid when the Mach number of the liquid flow is not small, such as immediately after bubble formation in water using optical breakdown (laser). Lauterborn & Vogel (2013) observed that, immediately after this bubble formation, an emitted shock wave detaches from the plasma surface at a velocity of approximately 4450 m s^{-1}, but soon it decays exponentially to the speed of sound in water within 140 ns. The newly formed bubble's surface expands with an initial velocity of approximately 2450 m s^{-1}, which also decays rapidly to approximately 250 m s^{-1} within 140 ns.

The second objective is to study the multi-oscillations of bubble dynamics near a rigid wall, which have not been modelled prior to the research contained herein. In reality, however, the oscillation usually takes at least a few cycles before the bubble breaks down into much smaller ones. In addition, it was suggested by the experimental studies (Tomita & Shima 1986; Philipp & Lauterborn 1998) that one of the major causes of cavitation erosion is associated with the second collapse. It is a bubble ring with high pressure and temperature in direct contact with a rigid boundary formed at the end of the second collapse. Our compressible model predicts the energy loss associated with the generation and propagation of shock waves at the end of collapse. Our computation traces jet impact, the transition of the bubble from a singly connected to a doubly connected form, and the recombining of a doubly connected to a singly connected form, and the further repeated transitions. The computational results of the bubble shapes correlate well with experimental data up to the end of the second oscillation.

2. Mathematical modelling

Consider gas bubble dynamics in an inviscid and compressible liquid near a rigid boundary. The maximum bubble radius R_m is chosen as the reference length, the density ρ_∞ in the undisturbed liquid as the reference density. The reference pressure is $\Delta p = p_\infty - p_v$, where p_∞ is the hydrostatic pressure in the undisturbed liquid and p_v is the partial pressure of vapour of the bubble. The reference velocity is thus obtained as $U = \sqrt{\Delta p/\rho_\infty}$. We introduce non-dimensional quantities indicated by asterisks as follows:

$$\boldsymbol{r}_* = \frac{\boldsymbol{r}}{R_m}, \quad t_* = \frac{U}{R_m}t, \quad \varphi_* = \frac{\varphi}{R_m U}, \tag{2.1a,b,c}$$

$$c_* = \frac{c}{c_\infty}, \quad p_* = \frac{p - p_\infty}{\Delta p}, \tag{2.1d,e}$$

where $\boldsymbol{r}$ is the position vector, t is the time, φ is the velocity potential of the liquid and p is the pressure. The sound speed c is normalized by its value c_∞ in the undisturbed liquid. In the following discussion we refer to dimensionless quantities unless specified otherwise.

We introduce the bubble wall Mach number as

$$\varepsilon = \frac{U}{c_\infty}, \tag{2.2}$$

which is assumed to be small in the present study. This theory is thus valid for bubble dynamics in a weakly compressible liquid.

The highest speed of the liquid flow induced by non-spherical bubble dynamics is usually associated with the velocity of the bubble jet. The highest jet velocity measured is less than 150 m s^{-1} for cavitation gas bubble dynamics near a rigid boundary at $R_m = 1.45$ mm, with γ being in the range of $0.3 \leqslant \gamma \leqslant 3.0$ (Philipp & Lauterborn 1998), where γ is the dimensionless standoff distance of the bubble from the boundary, defined as

$$\gamma = \frac{s}{R_m}, \tag{2.3}$$

where s is the distance between the boundary and the bubble centre at the moment of formation. The corresponding Mach number of the highest jet velocity in this case is less than 0.1, as the sound speed in water is $\sim$1500 m s^{-1}.

It has been reported from many experiments in the literature that the maximum velocity of a boundary-induced jet is lower than 200 m s^{-1} at normal ambient pressure. The values of the maximum jet velocities in the literature include: (i) 120 m s^{-1} (at $\gamma = 3.08$ for bubbles with $R_m = 2$ mm; Lauterborn & Bolle 1975); (ii) 170 m s^{-1} (at $\gamma = 1.6$ and $R_m = 3.1$ mm; Shima *et al.* 1981); (iii) 130 m s^{-1} (at $\gamma = 0.9$ and $R_m = 3.5$ mm; Tomita & Shima 1986); (iv) 156 m s^{-1} (at $\gamma = 2.3$ and $R_m = 3.2$ mm; Vogel, Lauterborn & Timm 1989); and (v) 125 m s^{-1} (at $\gamma = 1.7$ and $R_m = 1.55$ mm; Brujan *et al.* 2001).

Recently, Brujan & Matsumoto (2012) successfully obtained images of the dynamics of a micrometre-sized cavitation bubble near a rigid boundary. They noticed that the maximum jet velocity for a micrometre-sized bubble is slightly smaller than that for a millimetre-sized bubble, most likely due to surface tension and the viscosity of the liquid surrounding the bubble. They reported that the maximum jet velocity for a bubble at $R_m = 150$ μm near a rigid boundary is in the range from 80 m s^{-1} (at $\gamma \approx 1$) to 130 m s^{-1} (for $\gamma \approx 3$).

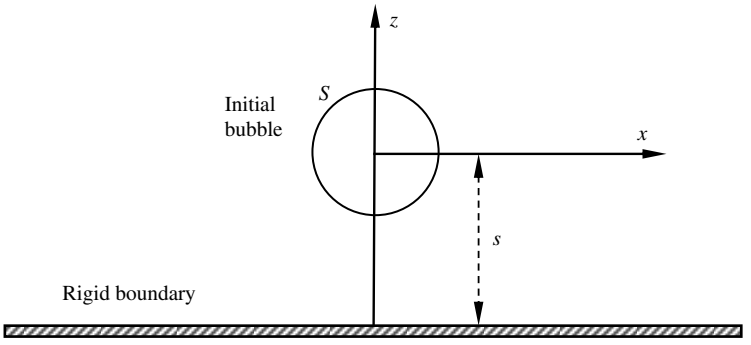

FIGURE 1. Illustration of a bubble near a rigid boundary, with a standoff distance s from the centre of the initial bubble to the boundary, and the coordinates used.

With the above discussion, we assume that the flow associated with cavitation gas bubble dynamics near a rigid boundary is subsonic, more specifically, a weakly compressible flow with a low Mach number. There are strong pressure impulses as the bubble nears its minimum volume, which are characterized by an abrupt and large change in the pressure in the liquid. These strong pressure impulses are often termed 'shock waves' in the field of bubble dynamics.

A Cartesian coordinate system is chosen, with the origin at the centre of the bubble at its inception $t = 0$, and the z-axis perpendicular to the rigid boundary, as illustrated in figure 1. The liquid flow at a low Mach number is governed by the equation of mass conservation,

$$\nabla_*^2 \varphi_* + \frac{\varepsilon^2}{c_*^2}\left(\frac{\partial p_*}{\partial t_*} + \boldsymbol{\nabla}_* \varphi_* \cdot \boldsymbol{\nabla}_* p_*\right) = O(\varepsilon^4), \tag{2.4a}$$

and the Bernoulli equation,

$$\frac{\partial \varphi_*}{\partial t_*} + \frac{1}{2}|\boldsymbol{\nabla}_* \varphi_*|^2 + p_* + \delta^2 z_* = O(\varepsilon^2), \tag{2.4b}$$

where $\delta = \sqrt{\rho g R_m / \Delta p}$ is the buoyancy parameter, with g the gravitational acceleration.

The kinematic material boundary condition on the bubble surface S is

$$\frac{\mathrm{d}\boldsymbol{r}_*}{\mathrm{d}t_*} = \boldsymbol{\nabla}_* \varphi_* \quad \text{on } S. \tag{2.5}$$

Assuming that the expansion and contraction of the bubble gas is adiabatic, the liquid pressure p_L on the bubble surface is given by

$$p_{L*} = p_{v*} + p_{g0*}\left(\frac{V_{0*}}{V_*}\right)^{\kappa} - \sigma_*\left(\frac{1}{R_{1*}} + \frac{1}{R_{2*}}\right) \quad \text{on } S, \tag{2.6}$$

where $p_{g0*} = p_{g0}/\Delta p$ is the initial partial pressure of the non-condensable gas content of the bubble, V_* is the bubble volume and V_{0*} is its initial value, κ is the ratio of the specific heats of the gas content, R_{1*} and R_{2*} are the principal radii of curvature of the bubble surface, and $\sigma_* = \sigma/(R_m \Delta p)$ is the surface tension coefficient.

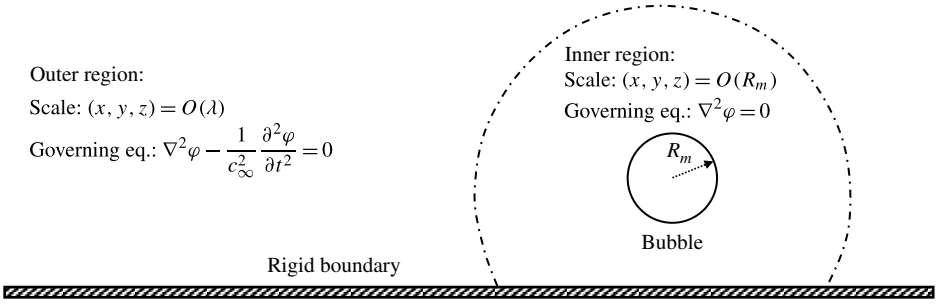

FIGURE 2. An illustration of the weakly compressible model for bubble dynamics near a rigid boundary with the collapse time T. The length scale $\lambda = c_\infty T$ at the far field is much larger than the maximum radius of the bubble R_m, where c_∞ is the speed of sound in the undisturbed liquid.

The dynamic boundary on the bubble surface and the boundary conditions on the rigid boundary and in the far field are, respectively, as follows:

$$\frac{\partial\varphi_*}{\partial t_*} + \frac{1}{2}|\nabla_*\varphi_*|^2 + p_{L*} + \delta^2 z_* = O(\varepsilon^2) \quad \text{on } S, \tag{2.7}$$

$$\varphi_{n*}|_{z_*=-\gamma} = 0, \tag{2.8}$$

$$\varphi_*|_{r_*\to\infty} = 0. \tag{2.9}$$

3. Matched asymptotic expansion

We divide the fluid domain into two regions: the inner region near the bubble, where $(x, y, z) = O(R_m)$; and the outer region far away from the bubble, where $(x, y, z) = O(c_\infty T)$, with $T = R_m/U$, as illustrated in figure 2.

The outer expansions in terms of the outer variable $\tilde{\boldsymbol{r}} = r/(c_\infty T) = \varepsilon \boldsymbol{r}_*$ is as follows:

$$\varphi_*(\boldsymbol{r}_*, t_*) = \phi(\tilde{\boldsymbol{r}}, t_*) = \phi_0(\tilde{\boldsymbol{r}}, t_*) + \varepsilon\phi_1(\tilde{\boldsymbol{r}}, t_*) + \cdots, \tag{3.1a}$$

$$p_*(\boldsymbol{r}_*, t_*) = P(\tilde{\boldsymbol{r}}, t_*) = P_0(\tilde{\boldsymbol{r}}, t_*) + \varepsilon P_1(\tilde{\boldsymbol{r}}, t_*) + \cdots. \tag{3.1b}$$

Substitution into (2.5a) and (2.5b) yields that the outer solutions of the first two orders satisfy the wave equation

$$\tilde{\nabla}^2\phi_i - \frac{\partial^2\phi_i}{\partial t_*^2} = 0 \quad \text{for } i = 0, 1, \tag{3.2}$$

where the operator $\tilde{\nabla}$ is defined in terms of $\tilde{\boldsymbol{r}}$.

One can obtain the outer solutions of the first two orders as follows:

$$\phi_0 = 0, \quad \phi_1 = \frac{F_1(t_* - \tilde{r})}{\tilde{r}}, \tag{3.3}$$

where F_1 is an arbitrary function to be determined by matching with the inner solutions.

The inner expansions in terms of the inner variable $\boldsymbol{r}_*$ are as follows:

$$\varphi_*(\boldsymbol{r}_*, t_*) = \varphi_0(\boldsymbol{r}_*, t_*) + \varepsilon\varphi_1(\boldsymbol{r}_*, t_*) + \cdots, \tag{3.4a}$$

$$p_*(\boldsymbol{r}_*, t_*) = p_0(\boldsymbol{r}_*, t_*) + \varepsilon p_1(\boldsymbol{r}_*, t_*) + \cdots. \tag{3.4b}$$

Substitution into (2.5*a*) and (2.5*b*) yields that the inner solutions of the first two orders satisfy Laplace's equation,

$$\nabla_*^2 \varphi_i = 0 \quad \text{for } i = 0, 1. \tag{3.5}$$

We thus may write their general solutions as follows, using the second Gauss identity:

$$\varphi_i(\boldsymbol{r}_*, t_*) = f_i(t_*) + \frac{1}{4\pi}\int_S \left(\frac{\partial \varphi_i(\boldsymbol{q}, t_*)}{\partial n} G(\boldsymbol{r}_*, \boldsymbol{q}) - \varphi_i(\boldsymbol{q}, t_*) \frac{\partial G(\boldsymbol{r}_*, \boldsymbol{q})}{\partial n} \right) \mathrm{d}S(\boldsymbol{q}) \quad \text{for } i = 0, 1, \tag{3.6}$$

where $f_i(t_*)$ for $i = 0, 1$ are arbitrary functions to be determined by matching with the outer expansion, $\boldsymbol{n}$ is the unit outward normal on the surface S, $\boldsymbol{q}$ is the integration variable on the surface S, and the Green's function is

$$G(\boldsymbol{r}_*, \boldsymbol{q}) = \frac{1}{|\boldsymbol{r}_* - \boldsymbol{q}|} + \frac{1}{|\boldsymbol{r}_* - \boldsymbol{q}_{im}|}, \tag{3.7}$$

with $\boldsymbol{q}_{im}$ the image of the source point $\boldsymbol{q}$ to the rigid boundary.

The outer limit of the inner expansion to second order can be obtained using (3.6) and (3.7) as

$$(\varphi_*)^o = f_0(t_*) + \frac{1}{2\pi}\frac{m_0(t_*)}{r_*} + \varepsilon f_1(t_*) + O(\varepsilon^2), \tag{3.8}$$

where $m_0(t_*)$ is the negative rate of the bubble volume,

$$m_0(t_*) = \int_S \frac{\partial \varphi(\boldsymbol{q}, t_*)}{\partial n} \mathrm{d}S(\boldsymbol{q}). \tag{3.9}$$

Using Van Dyke's matching principle (Van Dyke 1975) to match the inner and outer expansions yields

$$f_0(t_*) = 0, \quad f_1(t_*) = -\frac{m_0'(t_*)}{2\pi}, \quad F_1(t_*) = \frac{m_0(t_*)}{2\pi}, \tag{3.10}$$

where $m_0'(t_*)$ is the derivative of $m_0(t_*)$.

The far-field condition for the inner problem is obtained as

$$\varphi_*|_{r_*\to\infty} = \lim_{r_*\to\infty} (\varphi_*)^o = -\frac{\varepsilon m_0'(t_*)}{2\pi} + O(\varepsilon^2). \tag{3.11}$$

The combined inner solutions of the first two orders, $\varphi_*(\boldsymbol{r}_*, t_*) = \varphi_0(\boldsymbol{r}_*, t_*) + \varepsilon\varphi_1(\boldsymbol{r}_*, t_*)$, are thus governed by the following set of equations:

$$\nabla_*^2 \varphi_* = O(\varepsilon^2), \tag{3.12a}$$

$$\frac{\mathrm{d}\boldsymbol{r}_*}{\mathrm{d}t_*} = \nabla_* \varphi_* + O(\varepsilon^2) \quad \text{on } S, \tag{3.12b}$$

$$\frac{\partial \varphi_*}{\partial t_*} + \frac{1}{2}|\nabla_* \varphi_*|^2 + p_{L*} + \delta^2 z_* = O(\varepsilon^2) \quad \text{on } S, \tag{3.12c}$$

$$\varphi_{n*}|_{z_*=-\gamma} = 0, \tag{3.12d}$$

$$\varphi_*|_{r_*\to\infty} = -\varepsilon\frac{m_0'(t_*)}{2\pi} + O(\varepsilon^2), \tag{3.12e}$$

$$\varphi_{n*}|_{t_*=0} = -R_{t_*}(0) \quad \text{on } r_* = R_{0*}, \tag{3.12f}$$

where (3.12*a*)–(3.12*e*) are derived from (3.5), (2.6) and (2.8)–(2.10), respectively. Equation (3.12*f*) is the initial boundary condition, where we assume that it is a spherical bubble with radius R_{0*} and the bubble wall velocity at $R_{t*}(0)$.

The inner flow is of $O(1)$ and the outer flow $O(\varepsilon)$. This is as expected since the flow disturbance due to bubble dynamics is stronger in the inner region. Equations (3.12) are very similar to those of the incompressible model, but there are two essential differences: Laplace's equation (3.12*a*) is satisfied only in the inner region (whereas the governing equation in the outer equation is the wave equation), and the potential is with a non-zero term at the far field of the inner region as shown in (3.12*e*).

The non-zero term in (3.12*e*), $-\varepsilon m_0'(t_*)/(2\pi)$, is the combination effect of the bubble and its image to the rigid boundary. For a bubble in an infinite field or near a free surface, the corresponding far-field condition is $\varphi_*|_{r_*\to\infty} = -(\varepsilon/4\pi)m_0'(t_*) + O(\varepsilon^2)$.

By intuition, one would model the flow around the bubble as compressible and that in the far field as incompressible, since the flow velocity is higher in the inner region. The reason behind the present model is that the length scale R_m of the inner region is one order smaller than the length scale $\lambda = c_\infty T$ of the outer region,

$$\frac{R_m}{\lambda} = O\left(\frac{UT}{c_\infty T}\right) = O(\varepsilon), \tag{3.13}$$

whereas the time scales are the same for the two regions. Consequently, in the inner region, the second derivative of the potential in the time is two orders smaller than the second-order derivative of the potential in the space variables and the governing equation is approximated as Laplace's equation. In the outer region the two kinds of second-order derivatives are of the same order and the governing equation is the wave equation.

One can also think in the following way intuitively. The scale of the inner region is small compared with the wavelength of the acoustic wave. The pressure and velocity induced by the acoustic wave can be approximated as constant within the inner region to first order. In addition, the time scale T_a for the acoustic wave travelling across the inner region is much smaller than the collapse time T of the bubble,

$$\frac{T_a}{T} = O\left(\frac{R_{max}/C_\infty}{R_{max}/U}\right) = O\left(\frac{U}{C_\infty}\right) = O(\varepsilon). \tag{3.14}$$

The acoustic wave travels across the inner region instantly to first order. The inner flow can thus be assumed to be incompressible in the inner region to second order with the combined effects of the above two factors.

In general, the solution to Laplace's equation can differ by an arbitrary time-dependent constant and this constant is usually 'absorbed' into the potential. The m_0 term in (3.12*e*), a time-dependent constant, has to be explicitly considered since it is associated with the compressible effects, which describes the acoustic radiation of the energy of the bubble system to the far field. To verify this, we chose a large sphere

S_∞ with its origin at the centre of the initial bubble and with a radius R_∞, assuming $R_m \ll R_\infty \ll c_\infty T$. The energy flux across S_∞ is given by

$$E_{flux} = \oint_{S_\infty} \left(p_* + \frac{1}{2}\rho_* |\nabla_* \varphi_*|^2 \right) \varphi_{n*} \, \mathrm{d}s = - \oint_{S_\infty} \frac{\partial \varphi_*}{\partial t_*} \varphi_{n*} \, \mathrm{d}s + O(\varepsilon^2)$$
$$= -\frac{\varepsilon}{2\pi} m_0(t_*) m_0''(t_*) + O(\varepsilon^2), \tag{3.15}$$

where we have used $\varphi_* \to -\varepsilon m_0'(t_*)/(2\pi) + 1/(2\pi) m_0(t_*)/r_* + O(\varepsilon^2)$ as $r_* \to \infty$. There is a first-order energy flux to the far field of the inner region, which corresponds to the acoustic radiation.

4. Numerical modelling

4.1. *Boundary integral method*

To solve the initial boundary problem (3.12) using the usual BIM (cf. Wang *et al.* (1996*a*)), we make the following decomposition:

$$\varphi_* = \Phi - \varepsilon \frac{m_0'(t_*)}{2\pi}. \tag{4.1}$$

Substituting (4.1) into (3.12) yields

$$\nabla_*^2 \Phi = O(\varepsilon^2), \tag{4.2a}$$

$$\frac{\mathrm{d}\boldsymbol{r}_*}{\mathrm{d}t_*} = \nabla_* \Phi + O(\varepsilon^2) \quad \text{on } S, \tag{4.2b}$$

$$\frac{\mathrm{d}\Phi}{\mathrm{d}t_*} = \frac{1}{2}|\nabla_* \Phi|^2 - p_{L*} - \delta^2 z_* + \varepsilon \frac{m_0''(t_*)}{2\pi} + O(\varepsilon^2) \quad \text{on } S, \tag{4.2c}$$

$$\Phi_{n*}|_{z_*=-\gamma} = 0, \tag{4.2d}$$

$$\Phi|_{r_* \to \infty} = O(\varepsilon^2), \tag{4.2e}$$

$$\Phi_{n*}|_{t_*=0} = -R_{t*}(0) \quad \text{on } r_* = R_{0*}. \tag{4.2f}$$

Because Φ satisfies Laplace's equation (4.2*a*), its solution may be represented in terms of a boundary integral on the bubble surface S when the flow domain is in a singly connected form as follows:

$$\beta(\boldsymbol{r}_*, t_*)\Phi(\boldsymbol{r}_*, t_*) = \int_S \left(\frac{\partial \Phi(\boldsymbol{q}, t_*)}{\partial n} G(\boldsymbol{r}_*, \boldsymbol{q}) - \Phi(\boldsymbol{q}, t_*) \frac{\partial G(\boldsymbol{r}_*, \boldsymbol{q})}{\partial n} \right) \mathrm{d}S(\boldsymbol{q}), \tag{4.3}$$

where $\beta(\boldsymbol{r}_*, t_*)$ is the solid angle at the field point $\boldsymbol{r}_*$ at time t_*, under which the liquid domain is viewed from the field point $\boldsymbol{r}_*$. The solution (4.3) also satisfies the condition on the rigid boundary (4.2*d*) and the far-field condition (4.2*e*).

At each time step, we have a known bubble surface S and a known potential distribution Φ on the bubble surface. With this information we can calculate the tangential velocity on the bubble surface. The normal velocity on the bubble surface is obtained after solving the boundary integral equation (4.3). The bubble shape and the potential distribution on it can be further updated by performing the Lagrangian time integration of (4.2*b*) and (4.2*c*), respectively. The details on the numerical model using the BIM for the problem can be found in Taib (1985), Best (1994) and Wang *et al.* (1996*a*).

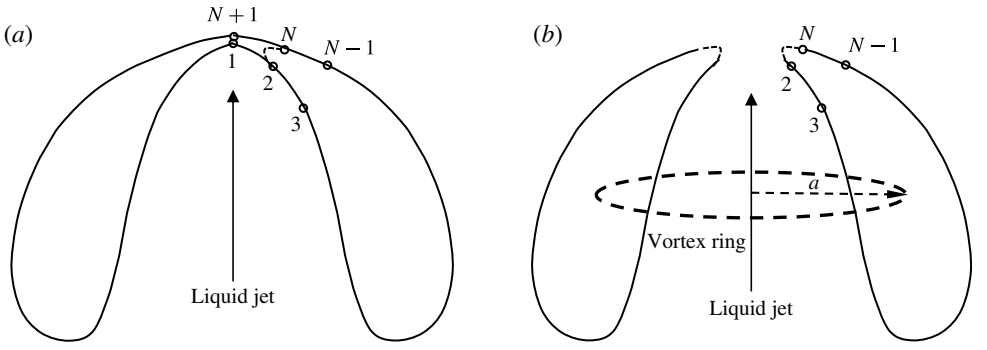

FIGURE 3. Illustration of the numerical transition of bubble shape and the vortex ring model: (*a*) immediately before and (*b*) immediately after jet impact, when a vortex ring is placed inside the toroidal bubble. The spatial distance between the nodal points has been exaggerated for clarity.

4.2. *Vortex ring model for toroidal bubbles*

A high-speed liquid jet often forms and subsequently penetrates through the bubble for non-spherical collapse. The liquid domain is then transformed from a singly connected to a doubly connected form, which results in non-uniqueness of the potential problem (4.2). The doubly connected domain can be made singly connected by using a vortex sheet (Zhang, Duncan & Chahine 1993; Zhang & Duncan 1994) or a branch cut (Best 1993). Pedley (1968) and Lundgren & Mansour (1991) modelled the dynamics of a bubble ring with a vortex ring inside, starting with a circular cross-section. Wang *et al.* (1996*b*, 2005) developed a vortex ring model from these earlier ideas to model the topological transition of a bubble and the subsequent toroidal bubble.

The numerical transition from a singly connected to a doubly connected bubble is activated when the distance between the jet tip to the opposite bubble surface is less than a prescribed small distance, which was chosen as $0.01R_m$ in the calculations in this paper. The bubble is then reconfigured in a very small neighbourhood of the impact point to a doubly connected bubble, as illustrated in figure 3. This is done artificially by removing the two nodes 1 and $N+1$ corresponding to the impact point and rejoining the bubble surface along the dashed line into a toroidal form.

In the vortex ring model, a vortex ring is placed inside the toroidal bubble once the jet impacts the opposite bubble surface, as shown in figure 3(*b*). The strength of the vortex ring is the circulation Γ_* of the flow along a closed path that threads through the toroidal bubble, which is a macroscopic measure of rotation of the liquid around the cross-section of the ring bubble. The circulation is equal to the jump of the potential φ_* across the contact point at the time of impact,

$$\Gamma_* = \oint_C \nabla_* \varphi_* \cdot \mathrm{d}\boldsymbol{r} = \varphi_{*N+1} - \varphi_{*1}, \tag{4.4}$$

where φ_{*1} and φ_{*N+1} are potentials at the impact point. The circulation is non-dimensionalized by $R_m U$. Here Γ_* is invariant in time when the potential satisfies Laplace's equation.

The potential φ_* is now decomposed as

$$\varphi_* = \phi_{vr} + \phi - \varepsilon \frac{m_0'(t_*)}{2\pi}, \tag{4.5}$$

where ϕ_{vr} is the potential of the vortex ring in the half-space bounded by the rigid boundary. With the potential jump being accounted for by the vortex ring using (4.5), the remnant potential ϕ is continuous in the flow field.

For an axisymmetric case, the vortex ring is a circle with its axis of symmetry along the z-axis. In theory, the precise location of the vortex ring (or loop) is immaterial so long as it lies completely within the toroidal bubble. To avoid possible numerical instability, the vortex ring should not be too close to the bubble surface. It is located at the farthest point from the bubble surface initially, and is relocated to the farthest inner point when it is within three element sizes from the bubble surface during the simulation. To find the farthest inner point approximately, we draw the Cartesian uniform grids (r_{ij}, z_{ij}) over an area that fully covers the bubble cross-section. We check if each of the grids is within the bubble cross-section and then sort out the farthest inner point from the inner grids by calculating their distance to all nodes on the bubble surface.

The induced velocity $\boldsymbol{v}_0^{vr}$ of a circular vortex ring of a radius a centred at the origin with unit strength can be calculated from the Biot–Savart law (cf. Yoon & Heister 2004)

$$\boldsymbol{v}_0^{vr}(r_*, z_*) = \frac{1}{4\pi}\oint_C \frac{\mathrm{d}\boldsymbol{l}(\boldsymbol{q}) \times (\boldsymbol{r}_* - \boldsymbol{q})}{|\boldsymbol{r}_* - \boldsymbol{q}|^3} = \frac{a}{2\pi d^3}\int_0^{\pi} \frac{\boldsymbol{i} z_* \cos\theta + \boldsymbol{k}(a - r_* \cos\theta)}{(1 - \eta\cos\theta)^{3/2}}\,\mathrm{d}\theta, \quad (4.6)$$

where C is the curve along the vortex ring, (r, z) are the cylindrical polar coordinates of the field point $\boldsymbol{r}_*$, $\boldsymbol{e}_r$ and $\boldsymbol{e}_z$ are the corresponding unit coordinate vectors, and

$$d = \sqrt{r_*^2 + z_*^2 + a^2}, \quad \eta = 2ar_*/d^2. \quad (4.7)$$

The velocity field of a circular vortex ring of radius a and strength Γ, centred at $z_* = b$ on the z-axis near a wall at $z_* = -\gamma$, can be obtained by the method of images as follows:

$$\boldsymbol{v}_{vr}(r_*, z_*) = \Gamma_* \boldsymbol{v}_0^{vr}(r_*, z_* - b) - \Gamma_* \boldsymbol{v}_0^{vr}(r_*, z_* - b_1), \quad (4.8)$$

where $b_1 = b - 2\gamma$.

We will choose the potential ϕ_{vr} of the vortex ring to vanish at infinity, so that the remnant potential ϕ vanishes at infinity too. For this purpose, the potential ϕ_{vr} is obtained by the line integral of the velocity $\boldsymbol{v}_{vr}(r_*, z_*)$ from the far field to the point considered. The process is described as follows.

The potential of the vortex ring at node 1, (r_{*1}, z_{*1}), on the bubble surface can be calculated as

$$\varphi_{vr}(r_{*1}, z_{*1}) = \int_{-\infty}^{z_1} w_{vr}(0, z_*)\,\mathrm{d}z_* + \int_0^{r_{*1}} u_{vr}(r_*, z_{*1})\,\mathrm{d}r_*, \quad (4.9)$$

where $u_{vr}(r_*, z_*)$ and $w_{vr}(r_*, z_*)$ are the r- and z-components of $\boldsymbol{v}_{vr}(r_*, z_*)$. The first integral is from infinity to $(0, z_1)$ along the z-axis, and the second integral is from the point $(0, z_{*1})$ to the point (r_{*1}, z_{*1}) along the line $z_* = z_{*1}$. The first integral can be performed analytically with the following result:

$$\varphi_{vr}(r_{*1}, z_{*1}) = \frac{\Gamma_*}{2}\left(\frac{z_* - b}{\sqrt{(z_* - b)^2 + a^2}} - \frac{z_* - b_1}{\sqrt{(z_* - b_1)^2 + a^2}}\right) + \int_0^{r_{*1}} u_{vr}(r_*, z_{*1})\,\mathrm{d}r_*. \quad (4.10)$$

The potential of the vortex ring at node j, (r_{*j}, z_{*j}), on the bubble surface may be further obtained by integrating the velocity field,

$$\varphi_{vr}(r_{*j}, z_{*j}) = \varphi_{vr}(r_{*1}, z_{*1}) + \int_0^{s_j} \boldsymbol{v}_{vr}(r_*, z_*) \cdot \mathrm{d}\boldsymbol{l}, \tag{4.11}$$

where s_j is the arc-length parameter for the point (r_{*j}, z_{*j}). The remaining integrals in (4.10) and (4.11) are performed numerically.

Substituting (4.5) into (3.12), one can obtain the boundary value problem for the remnant potential ϕ as follows:

$$\nabla_*^2 \phi = O(\varepsilon^2), \tag{4.12a}$$

$$\frac{\mathrm{d}\boldsymbol{r}_*}{\mathrm{d}t_*} = \boldsymbol{v}_{vr} + \nabla_* \phi + O(\varepsilon^2) \quad \text{on } S, \tag{4.12b}$$

$$\frac{\mathrm{d}\phi}{\mathrm{d}t_*} = 1 - \boldsymbol{v}_{vr} \cdot (\boldsymbol{v}_{vr} + \nabla_* \phi) + \frac{1}{2}|\boldsymbol{v}_{vr} + \nabla_* \phi|^2 - p_{L*} + \varepsilon \frac{1}{2\pi} m_0''(t_*) + O(\varepsilon^2) \text{ on } S, \tag{4.12c}$$

$$\phi_{n*}|_{z_*=-\gamma} = 0, \tag{4.12d}$$

$$\phi|_{r_*\to\infty} = O(\varepsilon^2). \tag{4.12e}$$

The above governing equations for the remnant potential ϕ are in the same form as the equations (4.2) for the potential Φ for the pre-toroidal phase. Thus ϕ can be solved using the BIM approach developed for Φ.

5. Computational results and analyses

Philipp & Lauterborn (1998) carried out a series of carefully controlled experiments for cavitation gas bubble dynamics near a rigid boundary at various standoff distances, capturing the detailed behaviour with a high-speed camera. The maximum bubble radius in the experiment is $R_m = 1.45$ mm. The computational parameters corresponding to the experiment are chosen as $\kappa = 1.4$, $\varepsilon = 0.013$, $\sigma_* = 0.000\,51$, $R_*(0) = 0.1$, $R_{t*}(0) = 31$ and $p_{g0*} = 127$. The dimensional parameters are $\rho = 1000$ kg m^{-3}, $\sigma = 0.07$ N m^{-1}, $p_\infty = 98.07$ kPa, $p_v = 2.98$ kPa, $R(0) = 0.145$ mm, $R_t(0) = 307$ m s^{-1} and $p_{g0} = 12.1$ MPa. We will analyse the computational results for the three cases at $\gamma = 3.0$, 2.0 and 1.6 in this section, and compare with the experimental data in the next section. For clarity of expression, we will term the expansion and collapse of a bubble during the first cycle of oscillation as just expansion and collapse, while expansion and collapse during the second cycle will be termed rebounding and recollapse.

Figure 4 shows the bubble shapes at $\gamma = 3.0$. The bubble remains spherical during the expansion phase (figure 4*a*) and most of the collapse phase (figure 4*b*). At the end of the collapse phase, the bubble appears kidney-shaped and a liquid jet directed to the rigid boundary forms rapidly. At jet impact on the opposite bubble surface, the circulation around a closed path threading the bubble ring is $\Gamma_* = 4.37$.

After jet impact the bubble becomes toroidal and rebounds. As the bubble rebounds rapidly, the thin jet penetrates through the bubble, and the bubble appears funnel-shaped with a protrusion pointing to the rigid boundary (figure 4*c*). As the jet becomes very thin, the bubble rejoins into a singly connected form and rebounds continuously until reaching its second maximum volume (figure 4*d*). In the meantime

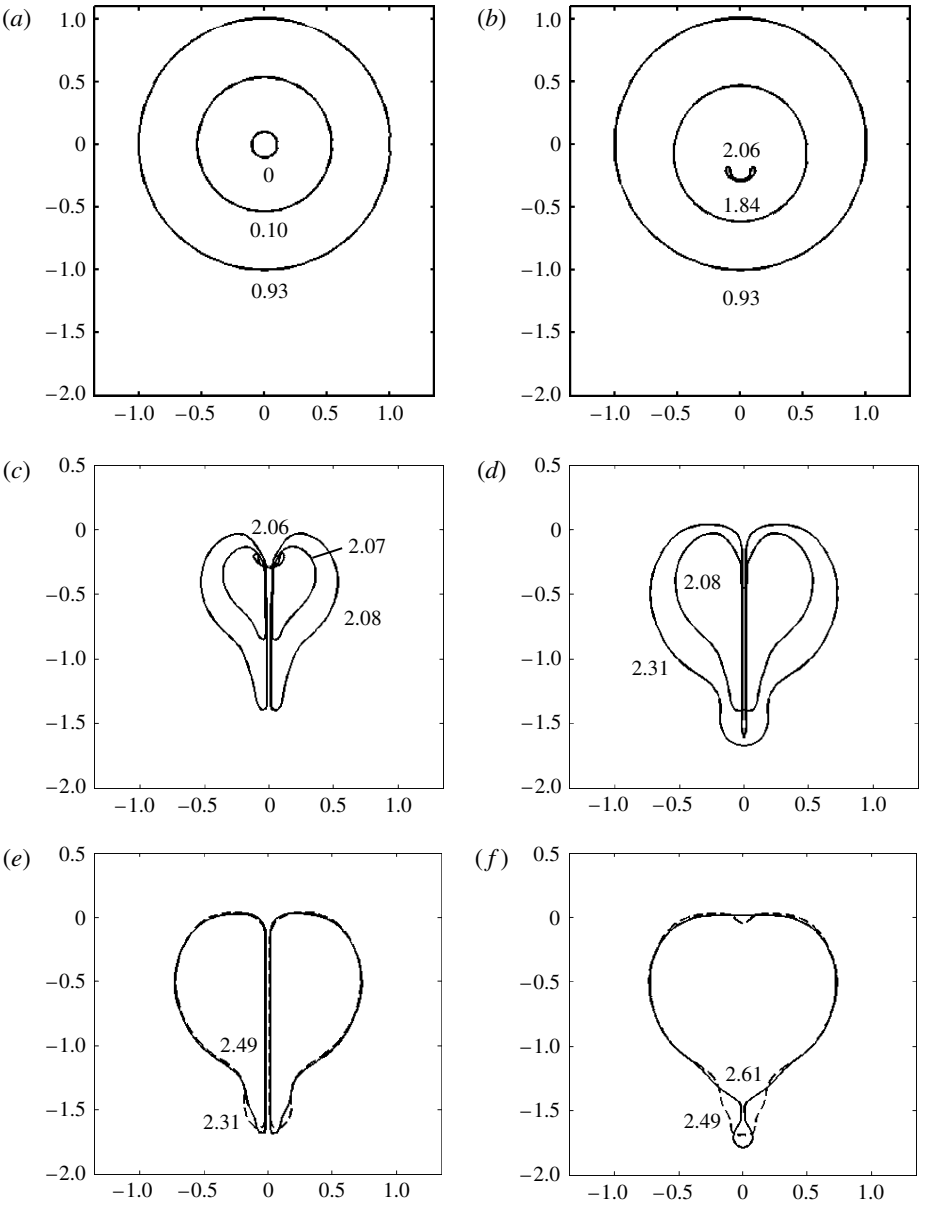

FIGURE 4. The motion of a bubble characterized by $\gamma = 3.0$, $\kappa = 1.4$, $\varepsilon = 0.013$, $\sigma_* = 0.00051$, $R_*(0) = 0.1$, $R_{t*}(0) = 31.0$ and $p_{g0*} = 127$. The bubble shapes are during (*a*) the first expansion phase, (*b*) the first collapse phase, (*c*,*d*) the second expansion phase in a doubly and singly connected form, respectively, and (*e*,*f*) the second collapse phase in a doubly and singly connected form, respectively.

the jet develops rapidly and penetrates the bubble again. After that, the bubble recollapses in a toroidal form for a short period (figure 4*e*). It then rejoins and recollapses in a singly connected form (figure 4*f*), with the protrusion part being separated from the main bubble. The repeated topological transitions occur from a

simply connected to a doubly connected form at $t_* = 2.06$ and 2.31, and from a doubly connected to a singly connected form at $t_* = 2.08$ and 2.49.

Figure 5 displays the bubble dynamics at $\gamma = 2.0$ with the rest of the parameters kept the same as in figure 4. Like in the last case the bubble remains nearly spherical during most of its first cycle of oscillation (figures 5*a* and 5*b*); however a wider jet develops earlier towards the end of the collapse phase. After jet impact the bubble collapses continuously in a toroidal form for a short period (figure 5*c*). It then rebounds in a toroidal form with a thin jet penetrating through it, leading to a funnel-shaped bubble (figure 5*d*). The bubble subsequently rejoins, rebounds in a singly connected form and its bottom part is flattened by the rigid boundary before it reaches its second maximum volume (figure 5*e*). It then recollapses, when the jet develops rapidly and repenetrates through the bubble (figure 5*f*). This time, the jet impinges on the rigid boundary as soon as it penetrates through the bubble. This high-speed jet impingement onto a boundary causes a high water hammer pressure of a short duration, which may cause damage to the boundary. After that the bubble recollapses continuously but in a toroidal form with its low surface retarded by the rigid boundary (figure 5*g*). It lastly joins again and recollapses continuously (figure 5*h*). The contact area between the bubble and the boundary first increases slowly with the rebounding and then reduces slowly with the recollapse phase. The repeated topological transitions from a simply connected to a doubly connected bubble occur at $t_* = 2.01$ and 3.32, and from a doubly connected to a singly connected bubble at $t_* = 2.38$ and 3.62.

Figure 6 displays the bubble dynamics at $\gamma = 1.6$ with the rest of the parameters kept the same as in figure 4. The bubble again remains nearly spherical during most of its first cycle of oscillation (figure 6*a*,*b*). However, a much larger jet develops earlier at the end of the collapse phase as compared with the above two cases at $\gamma = 3.0$ and 2.0. After jet impact the bubble collapses in toroidal form for a short period (figure 6*c*). It then rebounds in a toroidal form in a funnel shape before its lower parts are flattened by the rigid boundary at the middle stage of the rebounding phase (figure 6*d*). It further rebounds in a singly and doubly connected form successively (figure 6*e*,*f*), reaching its second maximum volume. After that, the whole bubble recollapses towards the rigid boundary (figure 6*g*). The contact area between the bubble and rigid boundary increases during the rebounding phase but does not change significantly during the recollapse phase, being about the maximum horizontal cross-section of the bubble during the middle stage of the recollapse phase. Near the end of the recollapse phase a wide jet penetrates through the bubble and impacts upon the rigid boundary immediately. This results in a bubble ring at a minimum volume touching the boundary at the end of the recollapse phase (figure 6*h*), when the pressure and temperature of the bubble gas are very high since they increase inversely with the bubble volume. The high pressure and high temperature generated upon violent recollapse within the bubble ring in direct contact with the rigid boundary are able to directly act on the boundary.

We next consider the global behaviour of the bubble. Figure 7(*a*) shows the time history of the equivalent radius $R_{eq*} = \sqrt[3]{(3/(4\pi))V_*}$ of the bubble for the above three cases at $\gamma = 3.0$, 2.0 and 1.6, respectively. The maximum radius reduces significantly from the first to second cycles of oscillation, and so does the oscillation period. The first oscillation period reduces slightly with the standoff distance but the second oscillation period reduces significantly with the standoff distance. The bubble maximum radius at the second cycle decreases obviously with the standoff distance, reducing 31 %, 18 % and 10 % at $\gamma = 3.0$, 2.0 and 1.6, respectively. This is because,

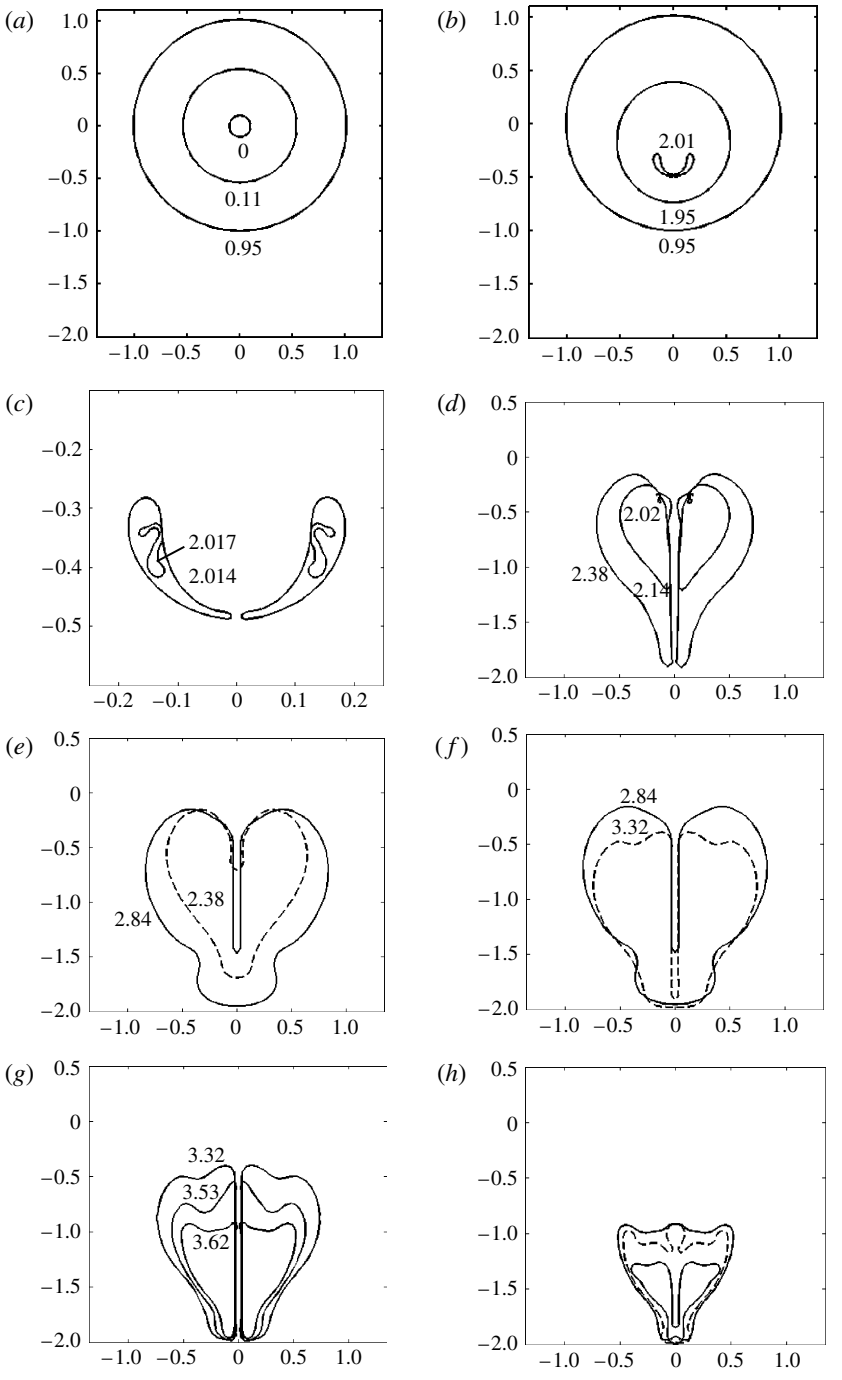

FIGURE 5. Bubble dynamics near a solid boundary at $\gamma = 2.0$, with the rest of the parameters the same as in the case shown in figure 4. The bubble shapes are during (*a*) the first expansion phase, (*b*,*c*) the first collapse phase in a singly and doubly connected form, respectively, (*d*,*e*) the second expansion phase in a singly and doubly connected form, respectively, and (*f*–*h*) the second collapse phase in a singly, doubly and singly connected form, respectively.

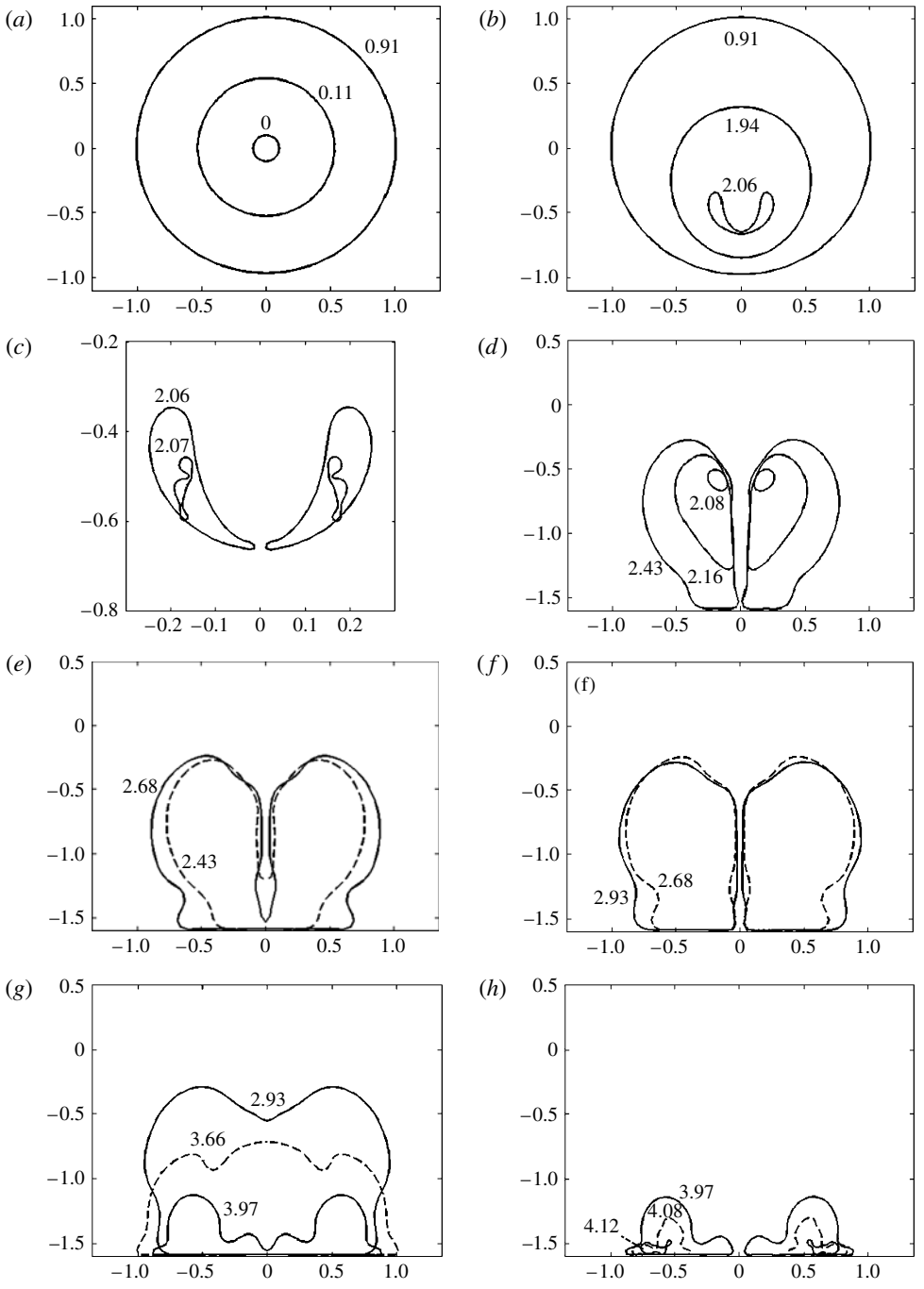

FIGURE 6. Bubble dynamics near a solid boundary at $\gamma = 1.6$, with the other parameters the same as in the case shown in figure 4. The bubble shapes are during (*a*) the first expansion phase, (*b*,*c*) the first collapse phase in a singly and doubly connected form, respectively, (*d*–*f*) the second expansion phase in a doubly, singly and doubly connected form, respectively, and (*g*,*h*) the second collapse phase in a singly and doubly connected form, respectively.

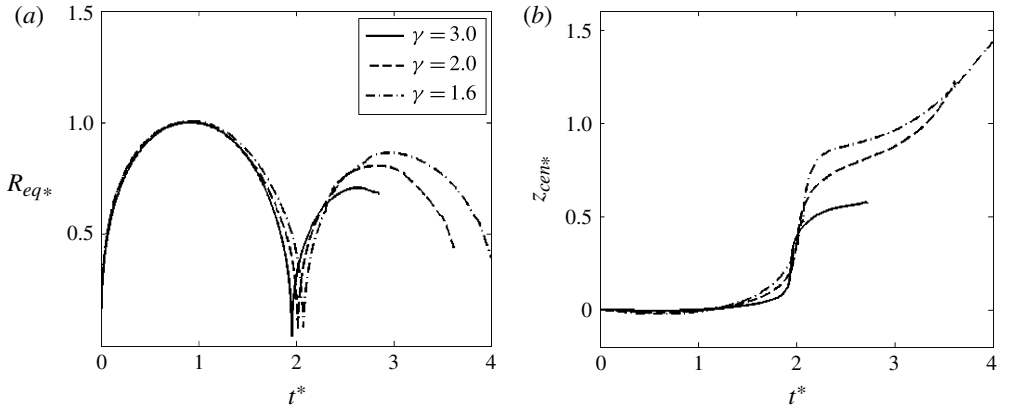

FIGURE 7. Histories for bubble dynamics near a rigid boundary at $\gamma = 3.0$, 2.0 and 1.6 for the cases shown in figures 4–6, respectively: (*a*) the bubble equivalent radius R_{eq*} and (*b*) the bubble centroid z_{cen*}.

when the bubble is closer to the rigid boundary, the bubble becomes non-spherical earlier, and a larger jet forms and a larger portion of kinetic energy is associated with the jet. Consequently, the bubble collapse becomes relatively weaker and less energy is radiated through the acoustic wave to the far field at the end of the collapse phase.

Figure 7(*b*) shows the corresponding time histories of the bubble centroid z_{cen*}. The bubble migrates to the rigid boundary and migrates faster at a smaller standoff distance. The migration speed reaches the maximum when the bubble is at its minimum volume. This translation is accelerated obviously from the first to second cycles of oscillation. This leads to a reduced distance at the ends of the collapse phase and especially the recollapse phase, thereby increasing the damage capability of the pressure impulse and bubble jetting.

6. Validation of numerical modelling

6.1. *Bubble volume history*

The initial conditions for the compressible model are different from those for the incompressible model. The initial conditions can be represented in terms of three parameters, $R_{0*} = R_{0*}$, R_{t0*} and p_{g0*}, where R_{t0*} is the dimensionless initial bubble wall velocity. In the incompressible modelling, the initial conditions can be set as a small spherical bubble with the radius R_{00*} at zero bubble wall velocity; R_{00*} is obtained by a backward integration of the Rayleigh–Plesset equation (Best 1993).

Wang (2013) noticed that the initial zero bubble wall velocity cannot be set for the compressible modelling based on the Keller equation (Keller & Kolodner 1956),

$$\left(1-\varepsilon\frac{\mathrm{d}R_*}{\mathrm{d}t_*}\right)R_*\frac{\mathrm{d}^2R_*}{\mathrm{d}t_*^2}+\frac{3}{2}\left(1-\frac{1}{3}\varepsilon\frac{\mathrm{d}R_*}{\mathrm{d}t_*}\right)\left(\frac{\mathrm{d}R_*}{\mathrm{d}t_*}\right)^2 = \left(1+\varepsilon\frac{\mathrm{d}R_*}{\mathrm{d}t_*}\right)\left(-1+p_{g0*}\left(\frac{R_{0*}}{R_*}\right)^{3\gamma}\right)-3\gamma\varepsilon p_{g0*}\left(\frac{R_{0*}}{R_*}\right)^{3\gamma}\frac{\mathrm{d}R_*}{\mathrm{d}t_*}. \quad (6.1)$$

When the Keller equation is integrated backwards from given initial conditions, the bubble wall velocity may increase monotonically as the bubble radius decreases, and

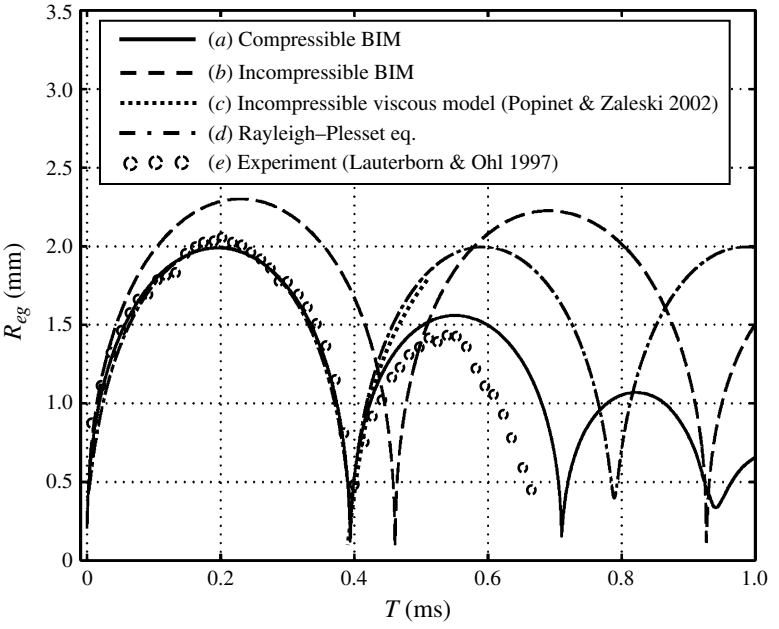

FIGURE 8. Comparison of the history of the bubble equivalent radius R_{eq} between (*a*) the compressible BIM model, (*b*) the incompressible BIM model, (*c*) the incompressible viscous model (Popinet & Zaleski 2002), (*d*) the Rayleigh–Plesset equation for a corresponding spherical bubble in an infinite liquid, and (*e*) the experiment (Lauterborn & Ohl 1997) for a bubble near a rigid wall at $R_m = 2$ mm, $\gamma = 2.45$. The initial conditions used for (*a*) and (*b*) are $R_0 = 0.2$ mm, $R_{t0} = 300$ m s^{-1} and $p_{g0} = 5$ MPa. The initial conditions used for (*c*) and (*d*) are $R_0 = 0.4$ mm, $R_{t0} = 0$ and $p_{g0} = 5.65$ MPa. The compressible initial conditions are used in (*d*) to emphasize the compressible effects neglected at the early expansion phase in this incompressible model.

increase rapidly as the radius is small. The backward integration does not achieve the zero bubble wall velocity as can be achieved with the incompressible modelling. With that in mind, the initial conditions for a compressible model should be set with a non-zero initial velocity of the bubble wall.

Figure 8 shows the comparison of the history of the equivalent bubble radius R_{eq} between the compressible BIM, the incompressible BIM and the experiment (Lauterborn & Ohl 1997) for a bubble near a rigid wall at $R_m = 2$ mm and $\gamma = 2.45$. This case was chosen because the experimental result for the history of the equivalent bubble radius was available, which was measured directly using a digital version of the photographic series and image processing techniques (Popinet & Zaleski 2002). The initial conditions for the compressible BIM are $R_0 = 0.2$ mm, $R_{t0} = 300$ m s^{-1} and $p_{g0} = 5$ MPa. Other parameters used for the calculation are $\rho = 1000$ kg m^{-3}, $\sigma = 0.07$ N m^{-1}, $p_\infty = 101$ kPa and $p_v = 2.98$ kPa. The compressible BIM predicts significant damping of oscillation of the bubble; its maximum radius and oscillation period reduce approximately 25 % from the first cycle to the second cycle of oscillation. There is approximately a 5 % discrepancy between the results of the compressible BIM and the experiment. This may be due to the viscous effects and heat transfer neglected in the model and/or the measurement errors in the experiment.

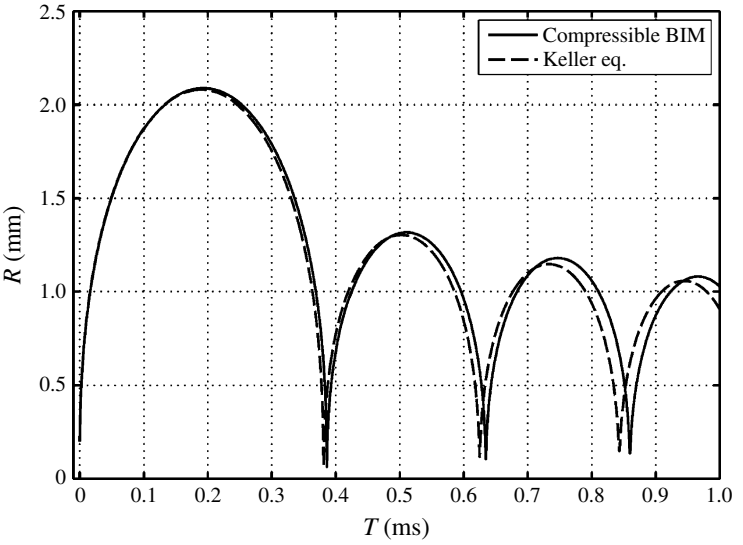

FIGURE 9. Comparison of the history of the bubble radius R for a spherical bubble starting at $R_0 = 0.2$ mm, $R_{t0} = 300$ m s^{-1} and $p_{g0} = 5$ MPa between the compressible BIM model and the Keller equation (Keller & Kolodner 1956).

The result for the incompressible BIM was obtained with the same initial conditions as the compressible BIM. The first maximum radius of the bubble obtained with this model is approximately 20 % larger than the experimental value, because the acoustic radiation to the far field due to the compressible effects at the early expansion phase was neglected in this model. This discrepancy can be corrected by setting the initial conditions for an incompressible model, such as the initial conditions used for the Rayleigh–Plesset equation to be given later on. The initial conditions for the compressible model used here are to show the energy loss of a bubble system due to acoustic radiation during both the early expansion and around the end of the collapse phase that is neglected in an incompressible model. The oscillation amplitude and period are almost the same during the first two cycles of oscillation since the compressible effects at the end of the collapse phase were neglected in the model.

The compressible effects neglected at the start of the first cycle of oscillation can be corrected by adjusting the initial conditions as shown in the result using the Rayleigh–Plesset equation for a spherical bubble in an infinite liquid with the initial conditions for the incompressible model: $R_0 = 0.4$ mm, $R_{t0} = 0$ and $p_{g0} = 5.65$ MPa. However the bubble undergoes undamped oscillation in the model.

Popinet & Zaleski (2002) calculated this case based on the incompressible Navier–Stokes equations with the viscosity coefficient for water chosen as 10^{-3} kg m^{-1} s^{-1}. Their model predicts well the radius history during the first cycle of oscillation but does not predict the significant damped oscillation observed in the experiment.

The compressible BIM successively predicts the acoustic radiation both at the beginning of the expansion phase and at the end of the collapse phase. Its agreement with the experiment indicates that the energy loss of a bubble system is primarily associated with acoustic radiation due to the compressible effects.

Figure 9 compares the compressible BIM and the Keller equation for the radius history $R(t)$ for a spherical bubble in an infinite liquid starting at $R_0 = 0.2$ mm, $R_{t0} = 300$ m s^{-1} and $p_{g0} = 5$ MPa. The compressible BIM agrees very well with the

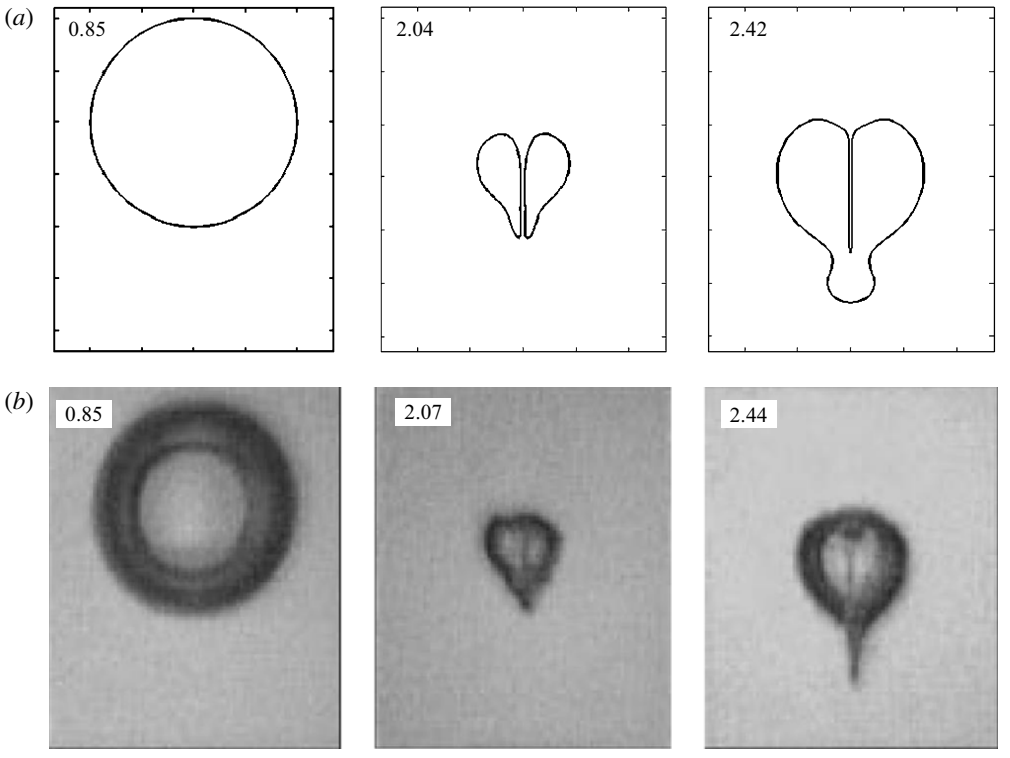

FIGURE 10. Comparison of (*a*) the BIM computation with (*b*) the experiment (reproduced with permission from Philipp & Lauterborn (1998)) for the bubble shapes at various dimensionless times for a cavitation bubble near a rigid boundary at $R_m = 1.45$ mm and $\gamma = 3.0$. The frame width is 3.9 mm for both the computational and experimental results.

Keller equation for more than three cycles of oscillation with small discrepancy. This confirms that the compressible BIM predicts the compressible effects at the same level of accuracy as the Keller equation for a spherical bubble, which in fact are both valid to the first two orders of $O(1)$ and $O(\varepsilon)$. The small difference should be due to the numerical errors in the BIM approach as well as the higher-order difference of $O(\varepsilon^2)$ between the two models. The first collapse that we call the 'principal collapse' is associated with the most significant energy being lost to the far field through acoustic radiation. The 'principal collapse' is associated with a significant initial bubble wall velocity, a feature not present in subsequent rebounds, as the bubble wall velocity is small at the beginning of rebounds (Wang 2013).

6.2. *Bubble shape evolution*

Figure 10 shows the comparison of the bubble shapes of the present computation and the experiment (Philipp & Lauterborn 1998), for cavitation gas bubble dynamics near a rigid boundary at $R_m = 1.45$ mm and $\gamma = 3.0$. The computational results are in the upper row and the corresponding experimental results are in the lower row. The bubble shapes are compared at representative times with slight differences between the computation and experiment. At the first time sequence at the dimensionless time $t_* = 0.85$, the bubble reaches its first maximum volume and is approximately

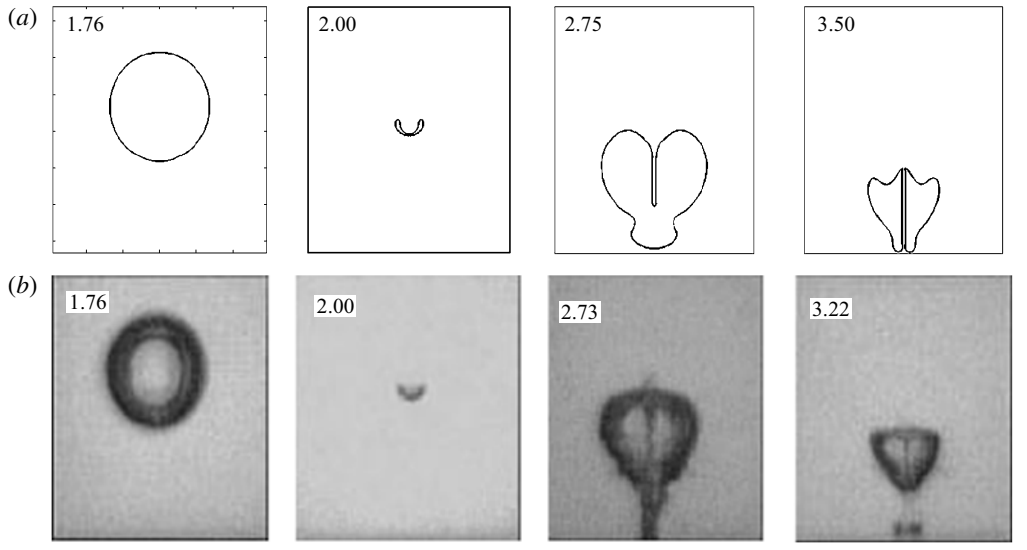

FIGURE 11. Comparison of (*a*) the BIM computation with (*b*) the experiment (reproduced with permission from Philipp & Lauterborn (1998)) for the bubble shapes at various dimensionless times for a cavitation bubble near a rigid boundary at $R_m = 1.45$ mm and $\gamma = 2.0$. The frame width is 3.9 mm for both the computational and experimental results.

spherical. The second time sequence at 2.04 is at the early stage of the rebounding phase, when the bubble takes a funnel shape with a thin jet penetrating through. At the third time sequence at 2.42, the bubble reaches its second maximum volume. The overall bubble shapes of the calculation and experiment are correlated except for at the end of the rebounding phase, when the protrusion in the experiment is much sharper. The potential cause for thicker protrusion in the computation should be due to the artificial joining and the subsequent numerical treatments, which assume that the bubble surface is smooth. In the experiment the jet does not disappear but disintegrates into tiny drops (Philipp & Lauterborn 1998), which cannot be simulated in the present model.

Figure 11 shows the comparison at $\gamma = 2.0$. The first time sequence at $t_* = 1.76$ is at the later stage of the collapse phase when the bubble is still spherical. The second time sequence at 2.00 is at the end of the first collapse phase, when a jet forms pointing to the rigid boundary. At the third time sequence at 2.75, the bubble reaches its second maximum volume, when the overall bubble shapes of the calculation and experiment are correlated. However, the protrusion in the experiment is much sharper, and the bubble in the computation is closer to the rigid boundary, with its protrusion being flattened by the boundary. The bubble migrates closer to the rigid boundary in the computation, either due to the viscous effects neglected in the computation and/or due to the measurement errors in the experiment (there is approximately 5 % deviation in the maximum radius in the experiment). The fourth time sequence at 3.50 is shortly before the end of the second collapse phase, when the bubble takes a funnel shape in both the computation and the experiment but the bubble in the calculation is nearer to the rigid boundary. As the bubble in the computation takes a larger maximum volume during the second cycle, the second oscillation period calculated is longer.

As observed in figure 11, the bubble in the computation is nearer to the rigid boundary during the rebounding phase than in the experiment. We thus compare in

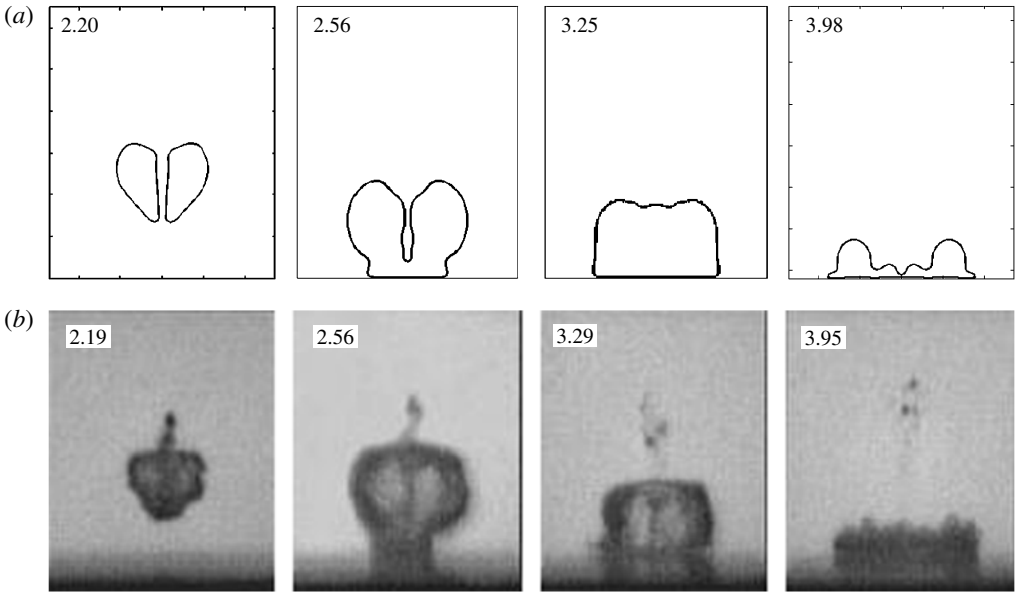

FIGURE 12. Comparison of (a) the BIM computation at $\gamma = 1.6$ with (b) the experiment at $\gamma = 1.4$ (reproduced with permission from Philipp & Lauterborn (1998)) for cavitation bubble dynamics near of a rigid boundary at $R_m = 1.45$ mm. The frame width is 3.9 mm for both the computational and experimental results.

figure 12 the bubble shapes between the computation at $\gamma = 1.6$ and the experiment at $\gamma = 1.4$ (Philipp & Lauterborn 1998), which are in good agreement. The first time sequence at $t_* = 2.20$ is at the early stage of the rebounding phase, when the bubble takes a funnel shape in both the computation and the experiment. At the second time sequence at 2.56, the bubble reaches its second maximum volume, when the low part of the bubble surface is flattened by the rigid boundary. The third sequence at 3.25 is at the middle stage of the recollapse phase, when the bubble takes an oblate cylinder shape standing on the boundary. The last sequence at 3.98 is at the end of the recollapse phase, when the bubble is like a pie on the boundary. All those features have been reproduced in the computation.

Figure 13(a) shows the bubble ring of the computation at $R_m = 1.45$ mm and $\gamma = 1.6$ in direct contact with the rigid boundary at the end of the recollapse phase (side view). Figure 10(b) shows the top view of the bubble ring (dashed lines) as well as the experimental image of the damaged area on an aluminium specimen caused by a repetition of 100 of the same bubbles nearby at $R_m = 1.45$ mm and $\gamma = 1.41$. The scale in panel (b) is the same as in panel (a). The damaged area is not symmetric due to the unavoidable slight asymmetry conditions in the experiment, but it is generally within the calculated bubble ring at the end of the recollapse phase. As an illustration, a laser beam can only generate an approximately spherical bubble.

7. Summary and conclusions

Bubble dynamics near a flat rigid boundary are associated with the generation of shock waves, a liquid jet and a vortex ring. The shock wave is a pressure impulse, but the associated liquid flow is usually subsonic with a small Mach number. Weakly

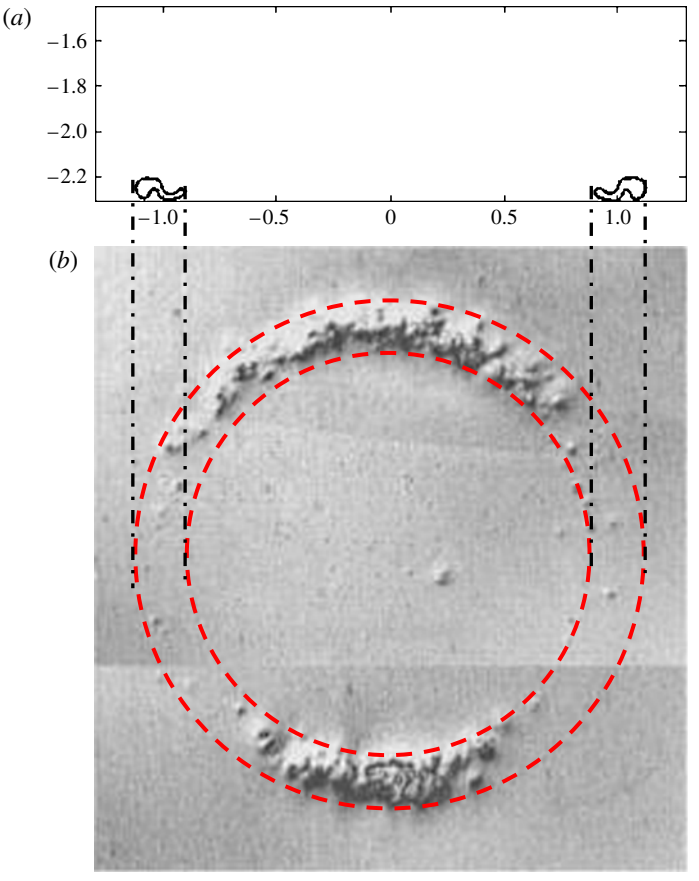

FIGURE 13. (Colour online) The bubble ring touches the rigid boundary at the end of the recollapse phase ($t = 0.616$ ms). (*a*) Side view of the bubble ring of the calculation at $R_m = 1.45$ mm and $\gamma = 1.6$. (*b*) Top view of the calculated bubble ring (dashed lines) and the damage on an aluminium specimen caused by 100 cavitation bubbles at $R_m = 1.45$ mm and $\gamma = 1.41$; frame width 2.6 mm (reproduced with permission from Philipp & Lauterborn (1998)).

compressible theory is thus implemented for this phenomenon using the method of matched asymptotic expansions in terms of the bubble–wall Mach number. As a result, the inner flow near the bubble to second order is described by Laplace's equation, with the compressible effects appearing only in the far-field condition. The problem is thus modelled approximately using the boundary integral method. The toroidal bubble formed towards the end of the collapse phase is modelled using a vortex ring model. The computation traces the repeated topological changes of the bubble from a singly connected to a doubly connected form, and vice versa.

This theory models the energy loss due to shock waves emitted both at the beginning of the expansion phase and at the end of the collapse phase. It thus predicts the significantly damped oscillation, where both the maximum bubble radius and oscillation period reduce significantly from the first to the second cycle of oscillation. The computational results of the bubble shapes correlate well with the experimental data to the end of the second cycle of oscillation for a bubble initiated

at various distances from the rigid boundary. The damping of the bubble oscillation is alleviated by the existence of the rigid boundary and reduces with the dimensionless standoff distance γ of the bubble from the rigid boundary. This is because, when the bubble is closer to the boundary, a larger jet forms and is associated with a larger amount of kinetic energy. Consequently, the collapse of the bubble is relatively weaker and less energy is radiated through the shock wave to the far field.

The bubble migrates to the rigid boundary and the migration speed is accelerated obviously from the first to the second cycle of oscillation. This leads to a reduced distance at the ends of the collapse phase and especially the recollapse phase, thereby increasing the damage capability of the shock wave and bubble jetting.

During the rebounding phase, a narrow jet penetrates through the bubble, and the bubble takes a funnel shape, with a long protrusion pointing to the rigid boundary. At $\gamma = 3.0$, the protrusion part intends to be separated from the main bubble at the early stage of the recollapse phase. At $\gamma = 2.0$, the protrusion touches the rigid boundary at the later stage of the rebounding phase. The bubble recollapses to the touching point subsequently. At $\gamma = 1.6$, the protrusion is flattened by the rigid boundary at the middle stage of the rebounding phase. The bubble recollapses to the rigid boundary and forms a bubble ring in contact with the boundary at the end of the recollapse phase. Some experiments suggested that the high pressure and temperature produced in the bubble ring in direct contact with the boundary at the end of the recollapse phase are the major cause of cavitation erosion of rigid materials (Tomita & Shima 1986; Philipp & Lauterborn 1998). The location of the bubble ring of our calculation correlates well with the damaged area on an aluminium specimen generated by a repetition of 100 of the same bubbles in the experiment (Philipp & Lauterborn 1998).

Acknowledgements

The author would like to express his sincere thanks to Professor John R. Blake and Professor Werner Lauterborn for valuable discussions and comments, as well as the associate editor for his valuable comments and suggestions during the refereeing process.

REFERENCES

ADOUA, R., LEGENDRE, D. & MAGNAUDET, J. 2009 Reversal of the lift force on an oblate bubble in a weakly viscous linear shear flow. *J. Fluid Mech.* **628**, 23–41.

BENJAMIN, T. B. & ELLIS, A. T. 1966 The collapse of cavitation bubbles and the pressure thereby produced against solid boundaries. *Phil. Trans. R. Soc. Lond.* A **260**, 221–240.

BEST, J. P. 1993 The formation of toroidal bubbles upon collapse of transient cavities. *J. Fluid Mech.* **251**, 79–107.

BEST, J. P. 1994 The rebound of toroidal bubbles. In *Bubble Dynamics and Interface Phenomena* (ed. J. R. Blake, J. M. Boulton-Stone & N. H. Thomas), pp. 405–412. Kluwer.

BLAKE, J. R. & GIBSON, D. C. 1987 Cavitation bubbles near boundaries. *Annu. Rev. Fluid Mech.* **19**, 99–123.

BLAKE, J. R., HOOTON, M. C., ROBINSON, P. B. & TONG, P. R. 1997 Collapsing cavities, toroidal bubbles and jet impact. *Phil. Trans. R. Soc. Lond.* A **355**, 537–550.

BLAKE, J. R., TAIB, B. B. & DOHERTY, G. 1986 Transient cavities near boundaries. Part 1. Rigid boundary. *J. Fluid Mech.* **170**, 479–497.

BLAKE, J. R., TAIB, B. B. & DOHERTY, G. 1987 Transient cavities near boundaries. Part 2. Free surface. *J. Fluid Mech.* **181**, 197–212.

BONHOMME, R., MAGNAUDET, J., DUVAL, F. & PIAR, B. 2012 Inertial dynamics of air bubbles crossing a horizontal fluid–fluid interface. *J. Fluid Mech.* **707**, 405–443.

BONOMETTI, T. & MAGNAUDET, J. 2007 An interface-capturing method for incompressible two-phase flows. Validation and application to bubble dynamics. *Intl J. Multiphase Flow* **33** (2), 109–133.

BRENNEN, C. E. 1995 *Cavitation and Bubble Dynamics*. Oxford University Press.

BRUJAN, E. A., KEEN, G. S., VOGEL, A. & BLAKE, J. R. 2002 The final stage of the collapse of a cavitation bubble close to a rigid boundary. *Phys. Fluids* **14** (1), 85–92.

BRUJAN, E. A. & MATSUMOTO, Y. 2012 Collapse of micrometre-sized cavitation bubbles near a rigid boundary. *Microfluid. Nanofluid.* **13**, 957–966.

BRUJAN, E. A., NAHEN, K., SCHMIDT, P. & VOGEL, A. 2001 Dynamics of laser-induced cavitation bubbles near elastic boundaries: influence of the elastic modulus. *J. Fluid Mech.* **433**, 283–314.

CALVISI, M. L., ILORETA, J. I. & SZERI, A. J. 2008 Dynamics of bubbles near a rigid surface subjected to a lithotripter shock wave: II. Reflected shock intensifies non-spherical cavitation collapse. *J. Fluid Mech.* **616**, 63–97.

CHAHINE, G. L. & BOVIS, A. 1980 Oscillation and collapse of a cavitation bubble in the vicinity of a two-liquid interface. In *Cavitation and Inhomogeneities in Underwater Acoustics* pp. 23–29. Springer.

CHAHINE, G. L. & HARRIS, G. 1988a Multi-cycle underwater explosion bubble model. Part I: Theory and validation examples for free-field bubble problems. *Report* IHCR 98-64. US Naval Surface Warfare Center, Indian Head Division.

CHAHINE, G. L. & HARRIS, G. 1988b Multi-cycle underwater explosion bubble model. Part II: Validation examples for hull girder whipping problems. *Report* IHCR 98-65. US Naval Surface Warfare Center, Indian Head Division.

CHAHINE, G. L. & PERDUE, T. O. 1988 Simulation of the three-dimensional behaviour of an unsteady large bubble near a structure. In *Proc. 3rd Intl Colloq. on Drops and Bubbles, Monterey, CA*.

COLE, R. H. 1948 *Underwater Explosions*. Princeton University Press.

COUSSIOS, C. C. & ROY, R. A. 2007 Applications of acoustics and cavitation to non-invasive therapy and drug delivery. *Annu. Rev. Fluid Mech.* **40**, 395–420.

CURTISS, G. A., LEPPINEN, D. M., WANG, Q. X. & BLAKE, J. R. 2013 Ultrasonic cavitation near a tissue layer. *J. Fluid Mech.* **730**, 245–272.

DELIUS, M. 1990 Effect of lithotripter shock waves on tissues and materials. In *Proc. 12th ISNA: Frontiers of Nonlinear Acoustics* (ed. M. F. Hamilton & D. T. Blackstock), pp. 31–46. Elsevier.

DUNCAN, J. H., MILLIGAN, C. D. & ZHANG, S. G. 1996 On the interaction between a bubble and a submerged compliant structure. *J. Sound Vib.* **197** (1), 17–44.

DUNCAN, J. H. & ZHANG, S. G. 1993 On the interaction of a collapsing cavity and a compliant wall. *J. Fluid Mech.* **226**, 401–423.

FENG, Z. C. & LEAL, L. G. 1997 Nonlinear bubble dynamics. *Annu. Rev. Fluid Mech.* **29**, 201–243.

GEERS, T. L. & HUNTER, K. S. 2002 An integrated wave-effects model for an underwater explosion bubble. *J. Acoust. Soc. Am.* **111**, 1584–1601.

GEERS, T. L., LAGUMBAY, R. S. & VASILYEV, O. V. 2012 Acoustic-wave effects in violent bubble collapse. *J. Appl. Phys.* **112**, 054910.

GEERS, T. L. & ZHANG, P. 1994 Doubly asymptotic approximations for submerged structures with internal fluid volumes. *Trans. ASME: J. Appl. Mech.* **61**, 893–906.

GUERRI, L., LUCCA, G. & PROSPERETTI, A. 1981 A numerical method for the dynamics of non-spherical cavitation bubbles. In *Proc. 2nd Int. Colloq. on Drops and Bubbles, California* NASA JPL Publications 82-7, p. 175 California Institute of Technology.

HERRING, C. 1941 The theory of the pulsations of the gas bubbles produced by an underwater explosion. *Report*. US National Defense Research Committee.

HUA, J. & LOU, J. 2007 Numerical simulation of bubble rising in viscous liquid. *J. Comput. Phys.* **222** (2), 769–795.

HUNG, C. F. & HWANGFU, J. J. 2010 Experimental study of the behaviour of mini-charge underwater explosion bubbles near different boundaries. *J. Fluid Mech.* **651**, 55–80.

ILORETA, J. I., FUNG, N. M. & SZERI, A. J. 2008 Dynamics of bubbles near a rigid surface subjected to a lithotripter shock wave: I. Consequences of interference between incident and reflected waves. *J. Fluid Mech.* **616**, 43–61.

JAYAPRAKASH, A., CHAO-TSUNG, H. & CHAHINE, G. 2010 Numerical and experimental study of the interaction of a spark-generated bubble and a vertical wall. *J. Fluids Engng* **134** (3), 031301.

JAYAPRAKASH, A., SINGH, S. & CHAHINE, G. 2011 Experimental and numerical investigation of single bubble dynamics in a two-phase bubbly medium. *J. Fluids Engng* **133**, 121305.

JOHNSEN, E. & COLONIUS, T. 2008 Shock-induced collapse of a gas bubble in shockwave lithotripsy. *J. Acoust. Soc. Am.* **124**, 2011–2020.

JOHNSEN, E. & COLONIUS, T. 2009 Numerical simulations of non-spherical bubble collapse. *J. Fluid Mech.* **629**, 231–262.

KELLER, J. B. & KOLODNER, I. I. 1956 Damping of underwater explosion bubble oscillations. *J. Appl. Phys.* **27** (10), 1152–1161.

KORNFELD, M. & SUVOROV, L. 1944 On the destructive action of cavitation. *J. Appl. Phys.* **15**, 495–506.

KLASEBOER, E., FONG, S. W., TURANGAN, C. K., KHOO, B. C., SZERI, A. J., CALVISI, M. L., SANKIN, G. N. & ZHONG, P. 2007 Interaction of lithotripter shockwaves with single inertial cavitation bubbles. *J. Fluid Mech.* **593**, 33–56.

KLASEBOER, E., HUNG, K. C., WANG, C., WANG, C. W., KHOO, B. C., BOYCE, P., DEBONO, S. & CHARLIER, H. 2005 Experimental and numerical investigation of the dynamics of an underwater explosion bubble near a resilient/rigid structure. *J. Fluid Mech.* **537**, 387–413.

LAUTERBORN, W. & BOLLE, H. 1975 Experimental investigations of cavitation-bubble collapse in the neighbourhood of a solid boundary. *J. Fluid Mech.* **72**, 391–399.

LAUTERBORN, W. & KURZ, T. 2010 Physics of bubble oscillations. *Rep. Prog. Phys.* **73**, 106501.

LAUTERBORN, W. & OHL, C. D. 1997 Cavitation bubble dynamics. *Ultrason. Sonochem.* **4**, 65–75.

LAUTERBORN, W. & VOGEL, A. 2013 Shock wave emission by laser generated bubbles. In *Bubble Dynamics and Shock Waves* (ed. C. F. Delale), pp. 67–103. Springer.

LEE, M., KLASEBOER, E. & KHOO, B. C. 2007 On the boundary integral method for the rebounding bubble. *J. Fluid Mech.* **570**, 407–429.

LEIGHTON, T. 1994 *The Acoustic Bubble*. Academic Press.

LENOIR, M. 1979 A calculation of the parameters of the high-speed jet formed in the collapse of a bubble. *J. Appl. Mech. Tech. Phys.* **20** (3), 333–337.

LESLIE, T. A. & KENNEDY, J. E. 2006 High-intensity focused ultrasound principles, current uses, and potential for the future. *Ultrasound Q.* **22**, 263–272.

LEZZI, A. & PROSPERETTI, A. 1987 Bubble dynamics in a compressible liquid. Part. 2. Second-order theory. *J. Fluid Mech.* **185**, 289–321.

LIND, S. J. & PHILLIPS, T. N. 2012 The influence of viscoelasticity on the collapse of cavitation bubbles near a rigid boundary. *Theor. Comput. Fluid Dyn.* **26** (1–4), 245–277.

LINDAU, O. & LAUTERBORN, W. 2003 Cinematographic observation of the collapse and rebound of a laser-produced cavitation bubble near a wall. *J. Fluid Mech.* **479**, 327–348.

LUNDGREN, T. S. & MANSOUR, N. N. 1991 Vortex ring bubbles. *J. Fluid Mech.* **72**, 391–399.

MINSIER, V., DE WILDE, J. & PROOST, J. 2009 Simulation of the effect of viscosity on jet penetration into a single cavitating bubble. *J. Appl. Phys.* **106**, 084906.

NAUDÉ, C. F. & ELLIS, A. T. 1961 On the mechanism of cavitation damage by non hemispherical cavities collapsing in contact with a solid boundary. *Trans. ASME D: J. Basic Engng* **83**, 648–656.

PEARSON, A., BLAKE, J. R. & OTTO, S. R. 2004 Jets in bubbles. *J. Engng Maths* **48** (3–4), 391–412.

PEDLEY, T. J. 1968 The toroidal bubble. *J. Fluid Mech.* **32**, 97–112.

PHILIPP, A. & LAUTERBORN, W. 1998 Cavitation erosion by single laser-produced bubbles. *J. Fluid Mech.* **361**, 75–116.

PLESSET, M. S. & CHAPMAN, R. B. 1971 Collapse of an initially spherical vapour cavity in the neighbourhood of a solid boundary. *J. Fluid Mech.* **47**, 283–290.

PLESSET, M. S. & PROSPERETTI, A. 1977 Bubble dynamics and cavitation. *Annu. Rev. Fluid Mech.* **9**, 145–185.

POPINET, S. & ZALESKI, S. 2002 Bubble collapse near a solid boundary: a numerical study of the influence of viscosity. *J. Fluid Mech.* **464**, 137–163.

PROSPERETTI, A. & LEZZI, A. 1986 Bubble dynamics in a compressible liquid. Part. 1. First-order theory. *J. Fluid Mech.* **168**, 457–478.

RAYLEIGH, LORD 1917 On the pressure developed in a liquid during the collapse of a spherical cavity. *Phil. Mag.* **34**, 94–98.

ROBERTS, W. W., HALL, T. L., IVES, K., WOLF, J. S., FOWLKES, J. B. & CAIN, C. A. 2006 Pulsed cavitational ultrasound: a noninvasive technology for controlled tissue ablation (histotripsy) in the rabbit kidney. *J. Urol.* **175**, 734–738.

SHIMA, A., TAKAYAMA, K., TOMITA, Y. & MIURA, N. 1981 An experimental study on effects of a solid wall on the motion of bubbles and shock waves in bubble collapse. *Acustica* **48**, 293–301.

SONG, W. D., HONG, M. H., LUK'YANCHUK, B. & CHONG, T. C. 2004 Laser-induced cavitation bubbles for cleaning of solid surfaces. *J. Appl. Phys.* **95** (6), 2952.

SZERI, A. J., STOREY, B. D., PEARSON, A. & BLAKE, J. R. 2003 Heat and mass transfer during the violent collapse of nonspherical bubbles. *Phys. Fluids* **15**, 2576–2586.

TAIB, B. B. 1985 Boundary integral method applied to cavitation bubble dynamics. PhD thesis, University of Wollonggong.

TAYLOR, G. I. 1942 Vertical motion of a spherical bubble and the pressure surrounding it. In *Underwater Explosion Research* vol. 2, pp. 131–144. Office of Naval Research.

TOMITA, Y. & SHIMA, A. 1986 Mechanisms of impulsive pressure generation and damage pit formation by bubble collapse. *J. Fluid Mech.* **169**, 535–564.

TURANGAN, C. K., JAMALUDDIN, A. R., BALL, G. J. & LEIGHTON, T. G. 2008 Free-Lagrange simulations of the expansion and jetting collapse of air bubbles in water. *J. Fluid Mech.* **598**, 1–25.

VAN DYKE, M. D. 1975 *Perturbation Methods in Fluid Mechanics*. 2nd edn. Parabolic Press.

VOGEL, A., LAUTERBORN, W. & TIMM, R. 1989 Optical and acoustic investigations of the dynamics of laser-produced cavitation bubbles near a solid boundary. *J. Fluid Mech.* **206**, 299–338.

VOGEL, A., SCHWEIGER, P., FRIESER, A., ASIYO, M. & BIRNGRUBER, R. 1990 Intraocular Nd:YAG laser surgery: damage mechanism, damage range and reduction of collateral effects. *IEEE J. Quantum Electron.* **26**, 2240–2260.

WANG, Q. X. 1998 The numerical analyses of the evolution of a gas bubble near an inclined wall. *Theor. Comput. Fluid Dyn.* **12**, 29–51.

WANG, Q. X. 2004 Numerical modelling of violent bubble motion. *Phys. Fluids* **16** (5), 1610–1619.

WANG, Q. X. 2013 Underwater explosion bubble dynamics in a compressible liquid. *Phys. Fluids* **25**, 072104.

WANG, Q. X. & BLAKE, J. R. 2010 Non-spherical bubble dynamics in a compressible liquid. Part 1. Travelling acoustic wave. *J. Fluid Mech.* **659**, 191–224.

WANG, Q. X. & BLAKE, J. R. 2011 Non-spherical bubble dynamics in a compressible liquid. Part 2. Acoustic standing wave. *J. Fluid Mech.* **679**, 559–581.

WANG, Q. X., YEO, K. S., KHOO, B. C. & LAM, K. Y. 1996*a* Nonlinear interaction between gas bubble and free surface. *Comput. Fluids* **25** (7), 607–628.

WANG, Q. X., YEO, K. S., KHOO, B. C. & LAM, K. Y. 1996*b* Strong interaction between buoyancy bubble and free surface. *Theor. Comput. Fluid Dyn.* **8**, 73–88.

WANG, Q. X., YEO, K. S., KHOO, B. C. & LAM, K. Y. 2005 Vortex ring modelling for toroidal bubbles. *Theor. Comput. Fluid Dyn.* **19** (5), 303–317.

WANG, S. P., ZHANG, A., LIU, Y. L. & ZENG, D. R. 2013 Numerical simulation of bubble dynamics in an elastic vessel. *Eur. Phys. J.* E **36**, 119.

WARDLAW JR., A. & LUTON, J. A. 2000 Fluid–structure interaction for close-in explosions. *Shock Vib. J.* **7**, 265–275.

WARDLAW JR., A., LUTON, J. A., RENZI, J. J. & KIDDY, K. 2003*a* Fluid–structure coupling methodology for undersea weapons. In *Fluid Structure Interaction II* pp. 251–263. WIT Press.

WARDLAW, A. B., LUTON, J. A., RENZI, J. R., KIDDY, K. C. & MCKEOWN, R. M. 2003*b* The Gemini Euler solver for the coupled simulation of underwater explosions. NSWCIHD/IHTR-2500.

YANG, B. & PROSPERETTI, A. 2008 Vapour bubble collapse in isothermal and non-isothermal liquids. *J. Fluid Mech.* **601**, 253–279.

YANG, Y. X., WANG, Q. X. & KEAT, T. S. 2013 Dynamic features of a laser-induced cavitation bubble near a solid boundary. *Ultrason. Sonochem.* **20**, 1098–1103.

YOON, S. S. & HEISTER, S. D. 2004 Analytical formulas for the velocity field induced by an infinitely thin vortex ring. *Int. J. Numer. Methods Fluids* **44**, 665–672.

YU, P. W., CECCIO, S. L. & TRYGGVASON, G. 1995 The collapse of a cavitation bubble in shear flows – a numerical study. *Phys. Fluids* **7** (11), 2608–2616.

YUE, P., FENG, J. J., BERTELO, C. A. & HU, H. H. 2007 An arbitrary Lagrangian–Eulerian method for simulating bubble growth in polymer foaming. *J. Comput. Phys.* **226** (2), 2229–2249.

YOUNG, F. R. 1989 *Cavitation*. McGraw-Hill.

ZHANG, S. G. & DUNCAN, J. H. 1994 On the non-spherical collapse and rebound of a cavitation bubble. *Phys. Fluids* **6** (7), 2352–2362.

ZHANG, S. G., DUNCAN, J. H. & CHAHINE, G. L. 1993 The final stage of the collapse of a cavitation bubble near a rigid wall. *J. Fluid Mech.* **257**, 147–181.